Prestressing of concrete using iron-based shape memory alloy (Fe-SMA) short fibers: Experimental and numerical analysis

Alireza Tabrizikahou[a,*], Mieczysław Kuczma[a], Zafiris Triantafyllidis[b], Moslem Shahverdi[b,c]

[a]Institute of Building Engineering, Poznań University of Technology, Piotrowo 5, Poznań 60-965, Poland
[b]Empa, Swiss Federal Laboratories for Materials Science and Technology, Überlandstrasse 129, Dübendorf 8600, Switzerland
[c]School of Civil Engineering, University of Tehran, Tehran 4563-11155, Iran

Abstract

Iron-based shape memory alloys (Fe-SMAs) exhibit unique shape recovery and memory effect behavior upon thermal activation, making them advantageous for structural applications such as prestressing. Introducing short Fe-SMA fibers into concrete structures allows for a uniform and localized distribution of prestressing forces within the concrete matrix. In this study, an experimental campaign was conducted to evaluate the efficiency of prestressing concrete using short Fe-SMA fibers. Concrete prism specimens reinforced with randomly dispersed Fe-SMA fibers, steel fibers, and plain concrete reference specimens were tested under three-point bending after exposure to ambient temperature, 160°C, and 200°C. All fiber-reinforced specimens contained a targeted 2% volume fraction of fibers with identical geometries featuring end-hooked shapes for enhanced pull-out resistance. At ambient temperature, the Fe-SMA fibers remain in a passive, non-activated state and do not undergo the phase transformation required to generate prestressing forces. As a result, at ambient temperature, specimens with steel fibers show higher flexural strength (22.95 MPa) than those containing Fe-SMA fibers (20.2 MPa). However, when the prisms with Fe-SMA fibers are heated to 160°C and 200°C, they recover their pre-defined shape, which applies prestress to the surrounding concrete. This prestress increases the load-bearing capacity of the prism, leading to higher flexural strength in the Fe-SMA specimens (26.65 MPa and 24.39 MPa, respectively) compared to their steel-fiber counterparts (19.46 MPa and 16.67 MPa, respectively). Based on these findings, a numerical model was developed to simulate the behavior of concrete composites reinforced with randomly dispersed Fe-SMA fibers. An algorithm was created to define the random distribution of fibers, and a novel modeling approach accounted for the end-hooked geometry by assigning different contact properties to the modeled straight fiber ends and middle sections. A mesh sensitivity analysis was performed to determine the optimal mesh size, and the model was validated by comparing numerical results with experimental data. In summary, the key finding of this work is that thermally activated Fe-SMA fibers can effectively prestress concrete and enhance its flexural strength beyond that achievable with conventional steel fibers at ambient conditions.

Keywords: Iron-based shape memory alloys (Fe-SMAs), prestressed concrete, thermal activation, fiber reinforcement concrete (FRC), experimental tests, numerical modeling

*Corresponding author
Email address: alireza.tabrizikahou@put.poznan.pl (Alireza Tabrizikahou)

Preprint submitted to Construction and Building Materials

1. Introduction

Fiber-reinforced concrete (FRC) is a composite material made of cementitious matrix and randomly distributed short, discontinuous fibers made from steel, glass, polymers, or natural fiber materials [1, 2, 3, 4]. FRC became popular in civil engineering applications due to its enhanced characteristics, which include greater flexural strength, ductility, fracture toughness, and durability [5, 6]. Fiber properties, volume fraction, shape, and orientation within the concrete mixture all have a significant impact on FRC performance [7, 8, 9]. Conventional FRC, including ultra-high-performance-FRC (UHPFRC), relies on steel or polymeric fibers to enhance mechanical properties such as tensile and flexural strength, toughness, and crack resistance [10, 11, 12]. While these fibers improve the post-cracking behavior of concrete, their contribution remains passive—fibers merely bridge cracks rather than actively restore or enhance structural performance. This passive nature limits their ability to provide additional functionalities such as self-centering, prestressing, or active crack closure.

In contrast to conventional steel fibers, shape memory alloy (SMA) fibers can provide unique capabilities due to their shape memory effect (SME) and/or superelastic properties (i.e. their ability to return to a pre-defined shape after large deformations) [13]. The SME occurs due to the reversible martensitic phase transformation in the alloy structure, inducing the unique behavior that is schematically shown in Figure 1. During loading and unloading, residual strain develops in the material. Heating the SMA above the austenite start temperature (A_s) initiates the transformation of twinned martensite into the austenite phase, which is completed at the austenite finish temperature (A_f). After cooling from the martensite start (M_s) to the martensite finish (M_f) temperatures, the austenite completely transforms back to twinned martensite. These critical temperatures are affected by the SMA's composition, manufacturing procedure, and applied stresses [14]. Over the last two decades, researchers have studied the integration of SMA wires and fibers, predominantly made of nickel-titanium (NiTi), into concrete composites [15]. Two main features of NiTi SMAs are leveraged in construction applications:

- Superelasticity and energy dissipation: At ambient temperatures, NiTi SMAs exhibit pseudoelastic (superelastic) behavior, which allows them to recover significant strains upon unloading while also providing improved energy dissipation and recentering capabilities. Several studies [16, 17, 18, 19, 20, 21, 22, 23] have demonstrated that incorporating superelastic NiTi bars or fibers into concrete elements can significantly improve their resilience to cyclic and seismic loading, resulting in self-centering structures with minimal permanent deformation [24, 25]. Experiments and simulations demonstrated that NiTi-reinforced concrete beams and bridge columns may recover a large amount of their deflection after unloading, lowering residual displacements and enhancing post-event performance [26, 27].

- Crack closing and prestressing: Beyond superelasticity, NiTi SMAs have the SME property, which allows them to revert to a pre-deformed shape when heated. Early research on SMA fiber-reinforced composites focused on employing heat activation to prestress, close, or reduce cracks in mortar and concrete specimens [28, 29, 30]. Several studies looked into embedding NiTi wires or short fibers in cementitious matrices to promote prestressing and crack closing when heated [31, 32, 23]. Such tests demonstrated partial or complete crack closure, resulting in increased durability and even enabling self-healing mechanisms by reducing crack width.

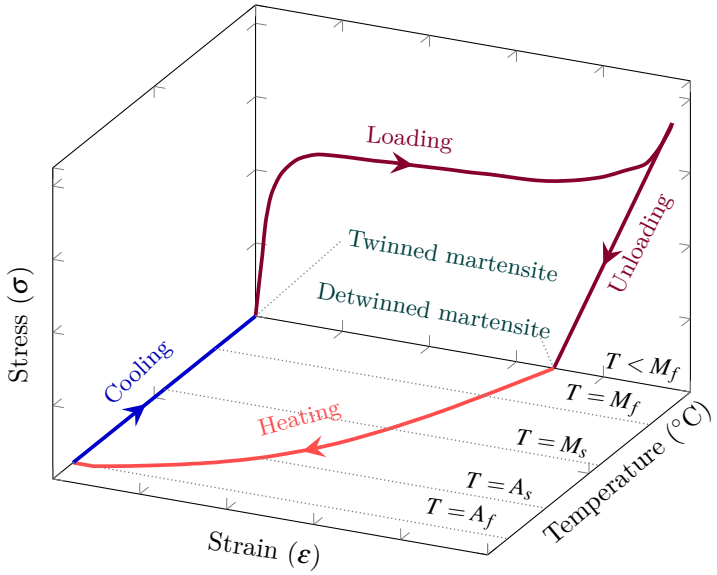

Figure 1: Shape memory effect of shape memory alloys [14].

Despite the promising results obtained with NiTi alloys, their high material costs, manufacturing complexity, and restricted scalability pose barriers to their widespread usage in civil engineering [33, 34]. In recent years, iron-based SMAs (Fe-SMAs) have developed as a less expensive and more scalable alternative [35, 36, 37]. Several investigations have shown that Fe-SMAs can be produced at a lower cost and with good workability while still providing acceptable SME for structural applications. Initially, research on Fe-SMAs concentrated on applications such as prestressed strengthening with Fe-SMA bars or strips applied externally or embedded in concrete. Shahverdi et al. [38, 39] determined that thermal activation of Fe-SMA strips and rods resulted in considerable prestress, enhancing load-bearing capacity and fatigue resistance in reinforced concrete beams. These investigations demonstrated the potential of Fe-SMAs for active strengthening and rehabilitation, however, they focused on large-scale reinforcing elements rather than short fibers dispersed throughout the concrete.

As of today, research on SMA fibers in concrete has primarily focused on NiTi alloys, with the goal of either leveraging superelasticity for energy dissipation or using SME for localized prestressing or crack closure. Very few research have looked into the ability of short SMA fibers to uniformly prestress concrete at the material level. Even fewer attempts have been made to employ Fe-SMA fibers, despite its cost, production, and scalability advantages. Previous research on Fe-SMA has focused primarily on bars, strips, or wires rather than small fibers randomly dispersed in a concrete matrix. Thus, there is a major gap in knowledge regarding:

- The performance of short Fe-SMA fibers as internal reinforcement in actively prestressed concrete.
- The measurement of mechanical advantages (e.g., improved flexural performance, increased fracture resistance) obtained from activating SME in short Fe-SMA fibers.

- The development of reliable numerical models capable of replicating Fe-SMA fiber dispersion, end-hooked shape, and interaction with the cementitious matrix.

This work aims to address these gaps by:

- Evaluating the feasibility and efficiency of integrating short, randomly dispersed Fe-SMA fibers directly into concrete mixtures, as opposed to prior investigations that used Fe-SMA bars or strips. By doing so, it aims to produce a more consistent, localized distribution of prestressing forces during thermal activation.
- Conducting an experimental campaign to investigate the behavior of Fe-SMA fiber-reinforced prisms at ambient and elevated temperatures (160°C and 200°C), comparing their flexural performance to steel-fiber-reinforced and plain concrete reference prisms. This method not only provides insights on mechanical improvements owing to SME activation, but it also creates a baseline for the temperature parameters necessary to cause prestress in a Fe-SMA fiber-reinforced system.
- Showing that short Fe-SMA fibers may actively prestress concrete and increase its load-bearing capacity, which is a significant step toward making SMA-FRC composites more economically viable for large-scale civil engineering applications. Fe-SMAs' lower cost and simplicity of production improve their potential for widespread adoption.
- Developing a numerical model, which includes randomized fiber distribution algorithms and novel modeling approaches for end-hooked geometries, allows for a better understanding of the underlying mechanics and provides guidelines for designing and optimizing Fe-SMA fiber-reinforced systems in the future.

Ultimately, this study introduces an innovative prestressing reinforcement concept using short Fe-SMA fibers and provides experimental data and numerical simulations to support its potential benefits. Section 2 provides detailed information on the materials used, the specimens preparation process, and the test methods used in the experiment. Section 3 presents the obtained results along with a discussion and interpretation of these findings. Section 4 describes the computational modeling procedures, including the generation of random fiber distributions, the constitutive material models utilized, contact properties, mesh sensitivity analysis, and validation of the simulations. Finally, Section 5 outlines the concluding remarks.

2. Experimental programme

2.1. Materials and specimens preparation

The investigations included two types of fiber materials: steel and Fe-SMA fibers. BEKAERT® 3D 65/35 steel fibers, measuring 35 mm in length and 0.55 mm in diameter (for an aspect ratio of 65), were used. According to the manufacturer's specifications (based on Datasheet Dramix 3D 6535BG EN-UK 20231204), these fibers have a tensile strength of 1,345 MPa and a Young's modulus of 210 GPa. The fibers were end-hooked, with a bent length of 6 mm and a width of 2 mm. Each cast specimen included 2.0% of these steel fibers in its volume. The components of the concrete mix are shown in Table 1. The concrete was poured into prism molds of $40 \times 40 \times 160$ mm^3, following EN 1015-11 testing standards [40]. The mixing procedures followed ASTM C192/C192M

specifications [41]. The formwork was removed 24 hours after casting, and specimens were placed in water at 20°C for 28 days before testing.

Table 1: Composition of high-performance concrete (HPC) mix used in the study [42].

Component	Amount in kg/m^3
Cement II 52.5R	620
Limestone powder	480
Fine sand (0-0.5 mm)	301
Coarse sand (0.5-1.0 mm)	708
Superplasticizer	16.5
Shrinkage reducing agent	16.5
Water	190

Figure 2 illustrates the form and geometry of the Fe-SMA fibers used in this study. The fibers are composed of Fe-17Mn-5Si-10Cr-4Ni-1(V, C) (mass%), with further details on their general properties available from Dong et al. [43] and Shahverdi et al. [39]. In addition, the specific Fe-SMA fiber material employed in this work was processed and heat-treated according to the optimal protocol identified in a recent study [44], involving annealing at 850°C for 2 hours. This heat treatment regimen, ensures the fibers develop the intended stress-strain behavior and recovery stress capacity. The fibers were produced from continuous spools of Fe-SMA wire with a diameter of 0.5mm. The wire was prestrained continuously to a strain level of 5.0%+/-1.0% over the whole length of each spool using a bespoke automated process. The prestrained wire was then passed through an industrial fiber cutting machine to crimp and introduce the permanent deformations for the hooked end regions, before cutting it to the final fiber length of 35mm. The Fe-SMA fibers had the same nominal length and similar aspect ratio with the commercial steel fibers used herein as a reference (L/D=70 and 65 for Fe-SMA and steel fibers, respectively), which was due to the unavailability of commercial steel fibers with the same length and diameter at the time of specimen fabrication.

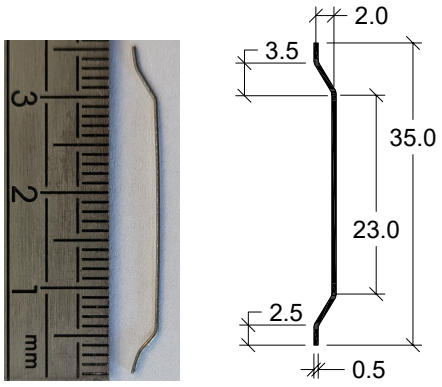

(a) (b)

Figure 2: The geometry of the Fe-SMA fibers (units are in millimeters) [42].

Three types of specimens were tested to determine the efficiency of prestressing concrete with short Fe-SMA fibers. The first type has a target volume fraction of 2.0% of Fe-SMA fibers. For comparison, a second batch of specimens included the same volume fraction of 2.0% of steel fibers, while a third type consisted of plain concrete with no fibers. A total of 18 specimens were cast for each type, resulting in 54 specimens overall. Since the application of Fe-SMA fibers in concrete requires thermal activation and exposure to high temperatures, three temperatures were included: ambient (no heating), 160°C, and 200°C. When heated to 160°C, the Fe-SMA material exhibits recovery stresses of about 350 MPa [39]. Other investigations suggest that increasing the activation temperature may partially enhance recovery stress levels [39, 45, 46, 47]. Consequently, this study for the sake of comparison, also included heating at 200°C. Each subcategory thus comprised six specimens. Considering these variables, multiple groups of specimens were prepared and tested. Table 2 details each type of specimen and the corresponding variable factors. Each category was labeled depending on the variable components used to help in the interpretation of the data. It is vital to note that the results reported in the following sections are based on the average outcomes of the six specimens in each category.

Table 2: Test matrix used for the experiments.

Material	Quantity	Activation Temperature (°C)	Specimen ID
Fe-SMA	6	Ambient	FRC-FeSMA-A
	6	160	FRC-FeSMA-160
	6	200	FRC-FeSMA-200
Steel	6	Ambient	FRC-Steel-A
	6	160	FRC-Steel-160
	6	200	FRC-Steel-200
Plain Concrete	6	Ambient	HPC-A
	6	160	HPC-160
	6	200	HPC-200

2.2. Test methods

2.2.1. Compressive and flexural tests

To evaluate the mechanical characteristics of the concrete and the impact of heating, both flexural and compressive strength tests were performed according to EN 1015-11 standards [40]. Initially, prism specimens measuring $40 \times 40 \times 160\,\text{mm}^3$ were cast and subjected to three-point bending tests to determine their flexural strength. Each prism was placed on two rolling supports spaced 100 mm apart, and a displacement-controlled load was applied at the mid-span (80 mm from either end) at a rate of 2.0 mm/min. During each test, both the displacement and the applied force at the loading point were recorded.

Following the flexural tests, the end segments of the prisms were cut to have cubic specimens measuring $40 \times 40 \times 40\,\text{mm}^3$ for compression testing. Specifically, six plain concrete prisms were cast for each temperature category, resulting in a total of 12 cubic specimens (two per prism), and hence 36 cubic specimens were tested in compression. These cubes were placed into compression platens with a $40 \times 40\,\text{mm}^2$ loading area and were tested under displacement-controlled loading at a rate of 2.0 mm/min. The average compressive strength values obtained from these specimens were used to characterize the concrete's properties under the different heating conditions. The results from both the flexural and compressive tests provided key input parameters for subsequent

analyses and computational simulations. Additionally, prism specimens reinforced with Fe-SMA and steel fibers were only tested in flexure. By comparing the results of these tests, the effectiveness of employing Fe-SMA fibers to prestress concrete could be assessed.

2.2.2. Thermal activation

Thermal activation is required to induce phase transformation in prestrained Fe-SMA materials, thereby enabling prestressing effects within the concrete. When these short Fe-SMA fibers are embedded and randomly distributed throughout the concrete, it is necessary to heat the entire composite to the target activation temperature. In this study, the heating process was carried out using a programmable heating chamber. Prism specimens designated for thermal activation (160°C and 200°C) were placed inside the chamber (see Figure 3), while reference prism specimens remained at ambient room temperature.

The heating chamber was programmed to increase the temperature at a rate of 8°C per minute until the desired setpoint (160°C or 200°C) was reached. Once the target temperature was attained, the chamber maintained it for the required duration. To monitor temperature distribution accurately, one additional dummy specimen (not used for subsequent mechanical testing) was cast and instrumented with thermocouples prior to heating. As illustrated in Figure 4, a K-type thermocouple was embedded in the core of this dummy prism specimen, and another was attached to its surface. These thermocouples were connected to a temperature data logger, allowing continuous, real-time tracking of both core and surface temperatures during the heating process. All other specimens designated for mechanical testing (flexural or compressive) were heated in separate but identically controlled batches without instrumentation. By ensuring the same heating rate and duration, the temperature profile measured in the dummy specimen was representative of the thermal conditions experienced by the tested specimens. Thus, the dummy specimen's temperature readings provided a reference to verify that the target activation temperature was reliably reached and maintained within the tested prisms. It was observed that sustaining the target temperature within the chamber for approximately 150–160 minutes enabled the core of the concrete to reach the desired activation temperature. This controlled heating approach ensured uniform thermal activation of the Fe-SMA fibers and served as a baseline for interpreting the prestressing behavior observed in the subsequent mechanical tests.

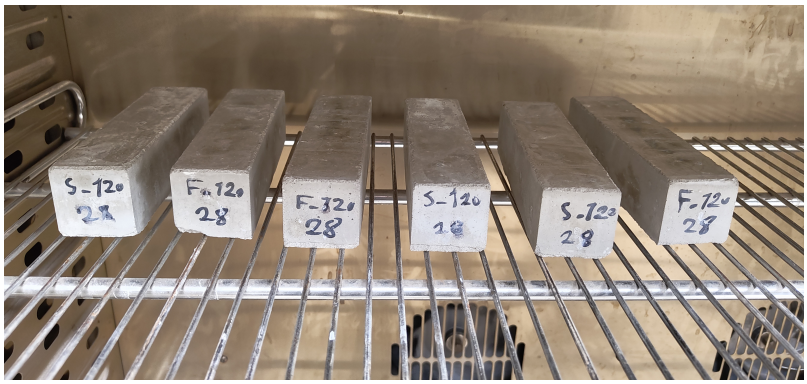

Figure 3: The prism specimens located inside the heating chamber for thermal activation [42].

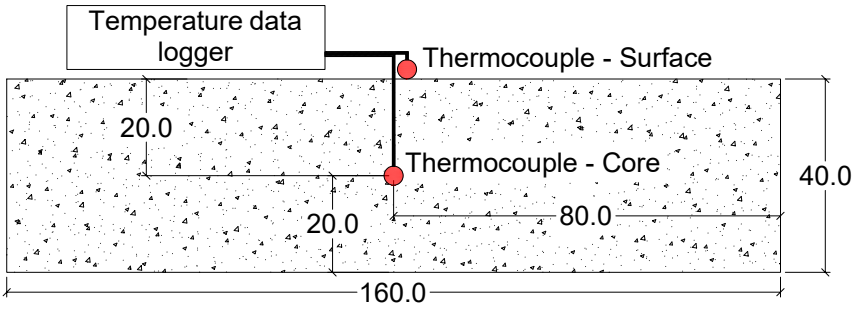

Figure 4: Schematic illustration of the thermocouple configuration used for temperature measurements in prism specimens (dimensions in millimeters) [42].

3. Results and discussion

Before presenting the results of the concrete prism tests, it is essential to establish a clear understanding of the thermomechanical behavior of the Fe-SMA fibers themselves. Since the prestressing of concrete using these fibers depends on their response to thermal activation and mechanical loading, dedicated tests were conducted on individual Fe-SMA fibers under conditions representative of the targeted heating scenarios. Characterizing the stress and strain response of the fibers at the chosen activation temperatures provides critical insight into their potential to generate recovery stress and prestressing forces. In this study, four prestrained end-hooked Fe-SMA fibers were subjected to controlled thermal and mechanical loading. For the thermal activation phase, each fiber was clamped at both ends and pre-loaded with approximately 100 MPa to prevent compression from heat-induced expansion during heating. Two temperature levels, 160°C and 200°C, were selected for activation: two fibers were heated to 160°C and the other two to 200°C. After reaching the target temperature, the fibers were cooled back to room temperature, and both stress values and chamber temperatures were continuously recorded.

Figure 5a illustrates the effects of this thermal cycle on the fibers. As the temperature increased from 24°C to 70°C, thermal expansion caused the stress to decrease significantly, settling between 10 MPa and 17 MPa. Upon reaching about 70°C, a slight stress increase was observed due to the phase transformation from martensite to austenite. For fibers heated to 200°C, the stress began to climb more rapidly after approximately 155°C. During cooling, the stresses in the fibers rose to about 360 MPa and 385 MPa for the 160°C and 200°C activation cases, respectively, indicating that raising the heating temperature from 160°C to 200°C could increase the recovery stress by approximately 25 MPa. Following the thermal activation, the mechanical performance of the fibers was evaluated under tensile loading. As shown in Figure 5b, the fibers—after being heated to either 160°C or 200°C—exhibited a nearly identical tensile behavior, sustaining strains up to around 30% and achieving an ultimate failure stress of approximately 1,150 MPa. This suggests that the mechanical properties of the Fe-SMA fibers remain largely unaffected by the prior thermal activation.

Figure 6 displays the stress-strain curves of the compressive behavior of plain concrete based on tests conducted on cubic specimens subjected to various temperatures. The specimens maintained at room temperature (HPC-A) exhibited the highest compressive strength of 98.35 MPa. When the plain concrete was exposed to 160°C (HPC-160), its compressive strength decreased to 71.7 MPa. This reduction in strength is consistent with the well-documented behavior of concrete at elevated temperatures, as thermal exposure above approximately 100°C often leads to microstructural

changes, loss of physically bound water, and potential damage to the cement paste and aggregate interfaces. Such effects are commonly observed to reduce not only compressive strength but also tensile and flexural properties, reflecting the material's sensitivity to heat-induced degradation. However, exposure to 200°C (HPC-200) resulted in an improvement in compressive strength to 95.39 MPa, which, while higher than the HPC-160 specimen, remained below the strength of the reference specimens kept at ambient temperature. The observed increase in compressive strength between 160°C and 200°C may be attributed to chemical reactions occurring within these temperature ranges, presenting an interesting phenomenon that suggests further investigation.

Figure 7 illustrates the flexural stress-strain responses of plain concrete specimens subjected to different temperature ranges. Among the tested specimens, those kept at ambient temperature (HPC-A) demonstrated the highest flexural strength, measuring 11.5 MPa. Exposure to 160°C (HPC-160) significantly reduced the flexural strength to 6.82 MPa. In contrast, specimens heated to 200°C (HPC-200) showed an enhanced flexural strength of 9.88 MPa. Although the HPC-200 specimens exhibited greater strength than the HPC-160 group, their flexural performance was still inferior to the ambient temperature reference specimens.

This trend, where the concrete subjected to 200°C shows a mechanical performance rebound compared to that heated to 160°C, is somewhat atypical for ordinary concrete. Generally, exposure to elevated temperatures above 100°C leads to progressive strength degradation due to factors such as the loss of physically and chemically bound water, micro-cracking at the aggregate–cement paste interface, and changes in the crystallinestructure of hydration products. However, certain HPCs and UHPCs have been reported to exhibit complex behavior under mild-to-moderate thermal exposure [48, 49, 50, 51]. In some UHPC formulations, sustained temperatures up to about 200°C may promote additional secondary hydration or microstructural rearrangements that temporarily enhance matrix densification and reduce porosity before severe microstructural damage sets in at higher temperatures. For instance, residual moisture within the pores might be released in a controlled manner, and ongoing pozzolanic reactions could fill previously open pores, leading to a short-term improvement in strength [52, 53]. It is important to note that this effect is not universally guaranteed and depends heavily on the specific material composition, the initial curing regime, and the presence of fine supplementary cementitious materials or reactive fillers. The particular mix design employed in this study may have facilitated a microstructural environment that allowed for these beneficial reactions or densification processes to occur at 200°C, temporarily offsetting the typical degradation seen at elevated temperatures.

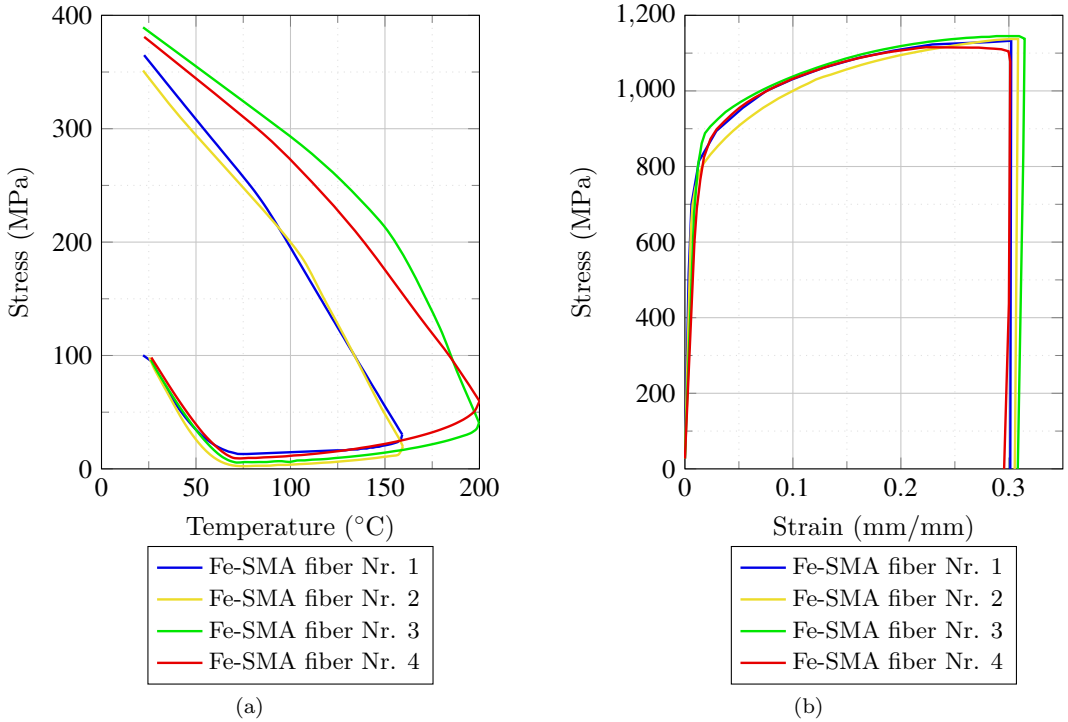

Figure 5: (a) Thermal activation process of pre-strained, and (b) tensile stress–strain (after thermal heating) of Fe-SMA fiber.

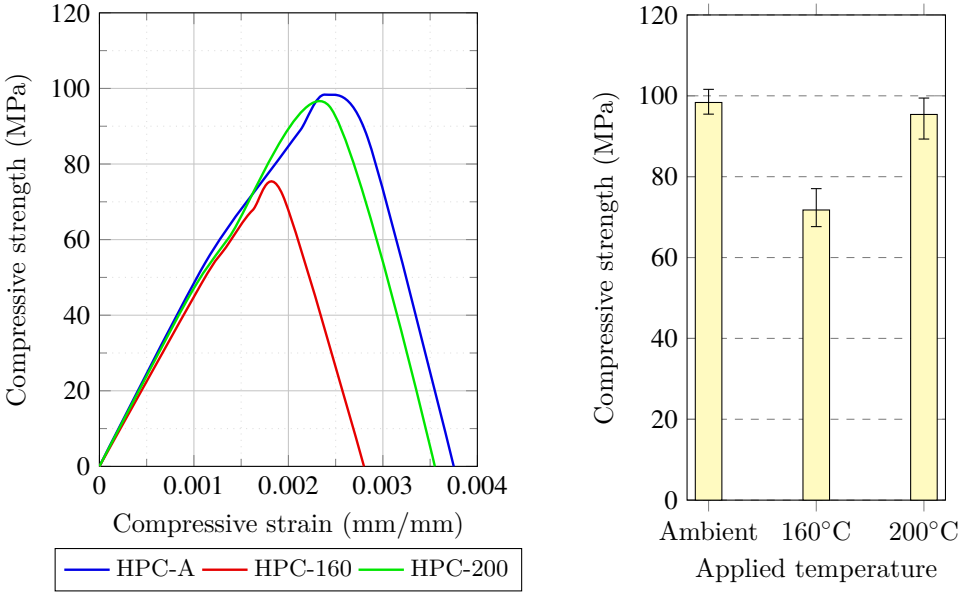

Figure 6: (a) Compressive stress–strain and (b) compressive strength of plain concrete subjected to different temperature conditions.

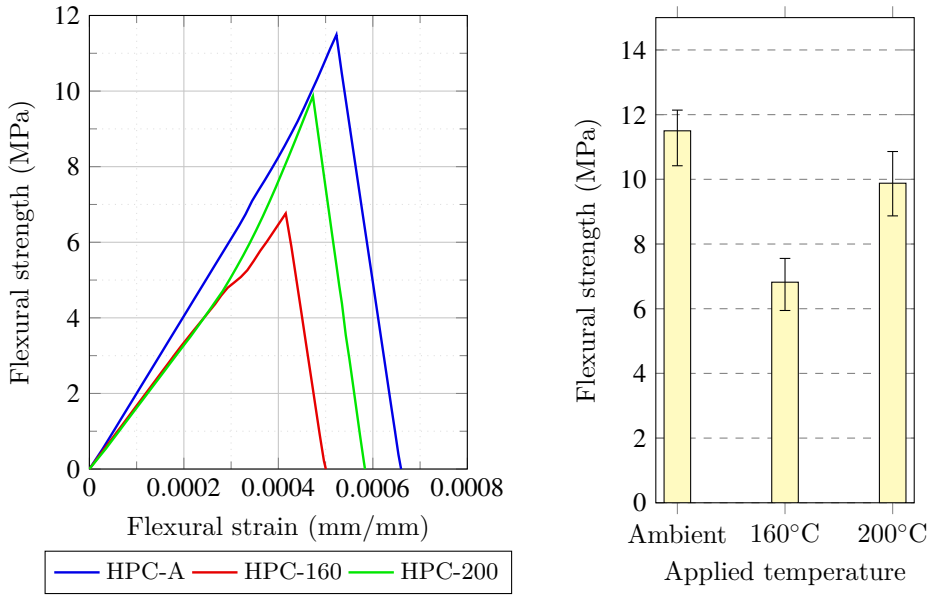

Figure 7: (a) Flexural stress–strain and (b) flexural strength of plain concrete subjected to different temperature conditions.

Figure 8 illustrates the flexural responses of prism specimens reinforced with Fe-SMA and steel fibers during a three-point bending test. Examining the behavior of specimens reinforced with steel fibers revealed a consistent decline in flexural strength as the applied temperature increased from ambient to 160°C and further to 200°C. Specifically, the flexural strength of the concrete-steel fiber composite decreased from 22.96 MPa at room temperature to 19.46 MPa at 160°C, and further to 16.67 MPa at 200°C. This reduction in performance can be attributed primarily to the thermal degradation of the concrete matrix and the resulting microcracking at higher temperatures. Since steel fibers do not undergo any phase transformation or generate recovery stresses upon heating, they remain passive reinforcements, much like non-prestrained Fe-SMA fibers would behave under similar conditions. Consequently, as the concrete's microstructure deteriorates at elevated temperatures, the pull-out resistance and load-carrying capacity of steel fibers diminish, leading to lower overall mechanical performance compared to the actively prestressed Fe-SMA fibers. Therefore, the elevated temperatures negatively impact the mechanical properties of the steel fibers and reduce their pull-out resistance within the concrete matrix [54, 54, 55, 56].

In contrast, specimens with Fe-SMA fibers showed a different response to thermal exposure. At ambient temperature, these specimens demonstrated a flexural strength of approximately 20.2 MPa. When heated to 160°C, the flexural strength increased to 26.65 MPa. This improvement is indicative of the phase transformation in Fe-SMA fibers triggered by thermal heating, which generates prestressing forces that are transferred to the surrounding concrete matrix. However, when the temperature is raised to 200°C, the flexural strength slightly decreases to 24.39 MPa. Although this value remains higher than that of the ambient-temperature specimens, it is slightly lower than the strength measured at 160°C. This response contrasts with the behavior of plain concrete spec-

imens, where an increase to 200°C resulted in higher flexural strength compared to 160°C. The observed decrease of flexural strength at 200°C in Fe-SMA-reinforced specimens may be due to a significant reduction in frictional forces and pull-out resistance between the concrete matrix and the Fe-SMA fibers. The thermal heating impacts not only the individual components, such as the concrete matrix and the fibers but also their interface, which plays a major role in the overall mechanical behavior. Therefore, careful consideration of thermal heating impacts is essential when utilizing Fe-SMA fibers for prestressing applications in concrete.

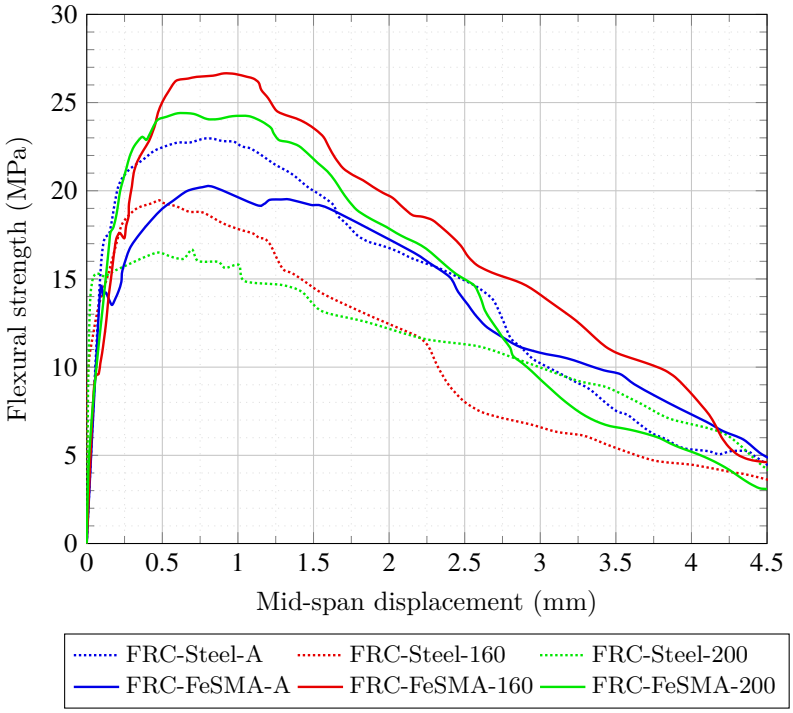

(a)

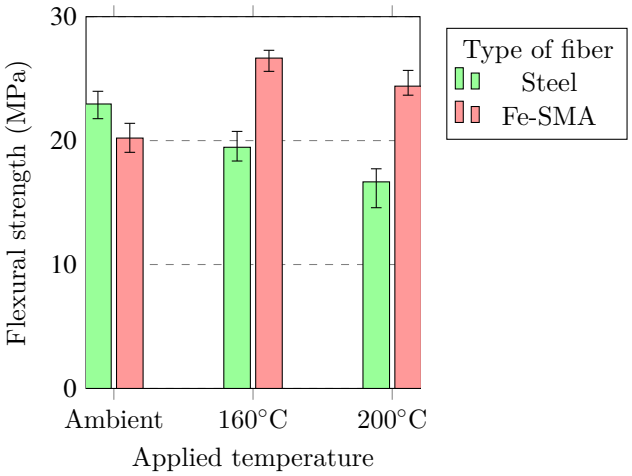

(b)

Figure 8: (a) Stress–strain curves and (b) flexural strength of specimens containing Fe-SMA and steel fibers subjected to different temperature conditions.

Figure 9 shows the crack propagation in specimens reinforced with Fe-SMA fibers during a three-point bending test. The initial stage captures the moment when the maximum flexural strength is

reached, at which point the first crack appears in the concrete. Notably, the crack does not form precisely at the mid-span but rather at a location exhibiting weaker strength. This variability may also be influenced by the specimen geometry. In this initial feasibility study, prisms with dimensions of 40 × 40 × 160 mm^3 were employed—dimensions commonly used for mortar testing. While suitable for the preliminary evaluation conducted here, the chosen prism size may not fully reflect the ideal conditions for random fiber dispersion, given the fiber length (approximately 35 mm). Future investigations involving larger or alternative specimen geometries could provide a more comprehensive assessment of the fiber distribution and mechanical behavior, further supporting the findings of this work. As the load increases, fiber pull-out in mid-span was observed, and the crack extends upward toward the top surface of the specimen, reaching the position of the loading gauge. Additionally, minor compressive forms of damage are visible at the support locations of the prism.

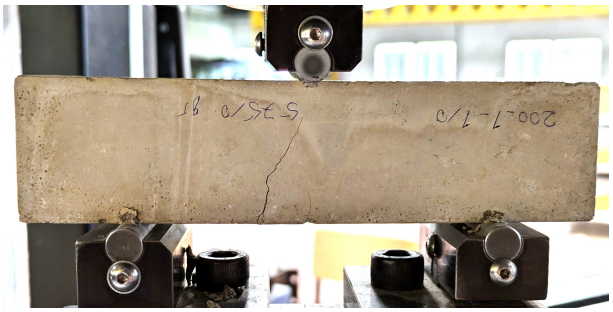

(a)

(b)

Figure 9: Three-point bending test for specimens reinforced with Fe-SMA fibers at (a) peak flexural stress and (b) failure.

Figure 10 presents the bottom view and crack opening of specimens reinforced with Fe-SMA fibers following three-point bending tests, categorized by the temperatures to which they were subjected. It is noteworthy that all specimens were photographed, and the observations discussed herein are based on the analysis of these images. For the sake of presentation, only three images are displayed in this study. An initial observation is the increase in the brightness of the concrete material with rising temperatures. This color change results from water evaporation and chemical reactions among the concrete constituents at elevated temperatures. Additionally, the fiber pull-out mechanism varied with temperature. In unheated concrete, the anchorage provided by the concrete matrix was sufficient to cause the end-hooks to straighten significantly before the fibers

were pulled out. At higher temperatures, however, increased microcracking and differential thermal expansion between the concrete and the fibers weakened this anchorage. As a result, the fibers were extracted more easily, with less hook straightening and reduced overall pull-out resistance. This behavior aligns with established knowledge regarding the negative impact of elevated temperatures on fiber-matrix bonding. In contrast, specimens exposed to 160°C and 200°C exhibited multiple fibers failing without significant straightening of their end-hooked geometries. This observation aligns with well-established findings in the literature, which indicate that as temperature increases, the concrete matrix undergoes microstructural changes that diminish the fiber–matrix bond and reduce pull-out resistance.

(a) (b) (c)

Figure 10: Bottom view and crack opening in specimens with Fe-SMA fibers exposed to (a) ambient (reference), (b) 160°C, and (c) 200°C temperature.

4. Computational modeling

4.1. Generation of the random distribution of fibers

It is critical to generate random fiber distributions within three-dimensional specimens to analyze fiber-reinforced concrete composites [57, 58]. Modeling these distributions allows for a more precise and reliable investigation of the mechanical characteristics of fiber-reinforced composites [59]. This section provides a brief introduction to a developed Python-based script that integrates with ABAQUS CAE to make it easier to develop models with randomly distributed short fibers.

Figure 11 depicts the developed script's process. This algorithm provides a reliable approach for modeling fiber placement within a composite prism, taking into account important factors such as settling effects, avoiding fiber overlap, and adhering to predetermined volume fractions over several layers. The algorithm's ability to modify parameters such as fiber diameters, tolerances, settling percentages, and volume fractions makes it suitable for a wide range of materials and applications.

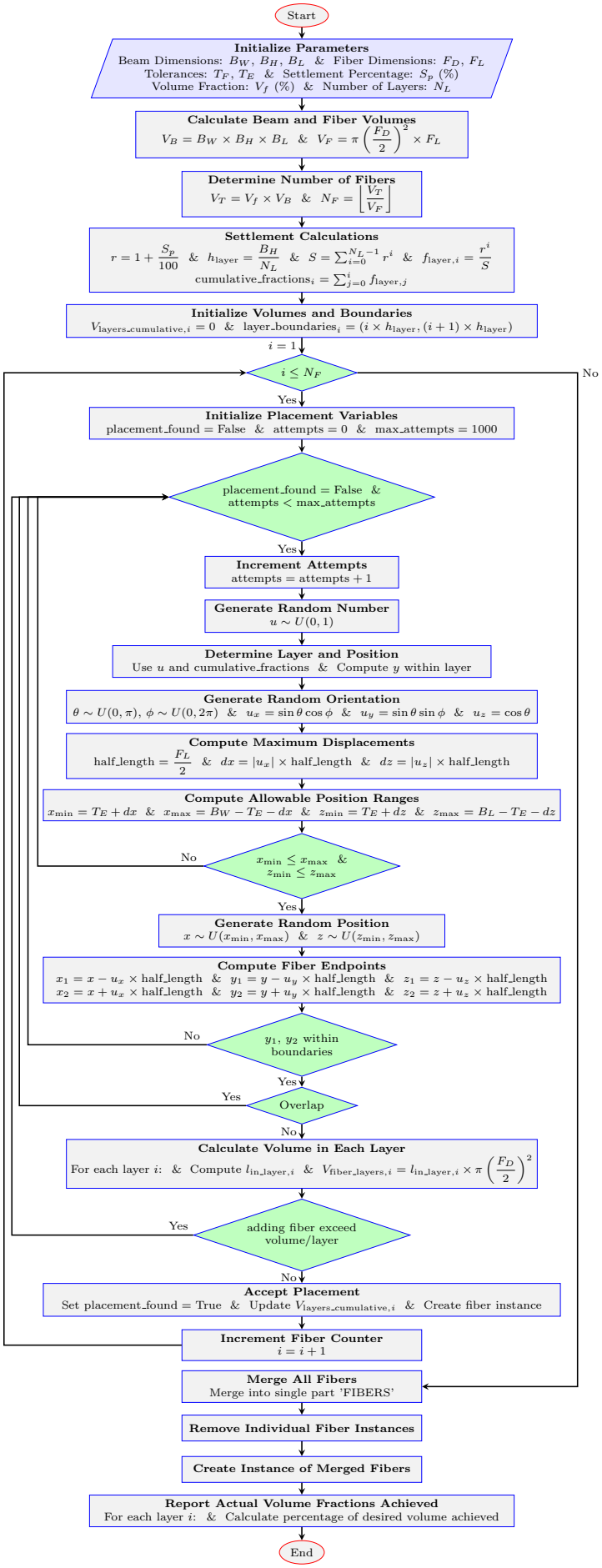

Figure 11: The procedure used to generate the random distribution of fibers inside a cubic or cylindrical specimen.

The provided experimental results (Section 3) are based on average results of tests carried out on multiple specimens (Section 2). Several models were developed and analyzed for computational investigations, and the average responses are shown in Section 4.4. Each time the script was executed, it generated a different random distribution of fibers within the prism specimen. As a result, six models were analyzed: three with no fiber settling and three with 5% fiber settlement. The settlement was distributed over four layers, with the fiber content increasing by 5% in each successive layer moving downward toward the bottom of the prism specimens. Figure 12 shows that the fibers in all six models are straight. To resemble the end-hooked geometry and distinguish the pull-out behavior between the straight and end-hooked parts, the fibers were divided into three segments: a middle straight section of 23mm and end sections of 6mm each, totaling 35mm, consistent with the experimental fibers. The partitioning was utilized to assign unique contact characteristics to each segment, as explained in Section 4.3.

The justification for classifying the models into those with and without fiber settling originates from observations made during casting and testing. It was discovered that a small fraction of fibers settled while the concrete mix was still fresh and not hardened. Mechanical testing of the prism specimens found that fiber settlement occurred in the mid-span, where cracking was visible, with settlement percentages ranging from 3% to 8%. Although this range may appear small, the current study included fiber settling in the modeling to determine its possible influence on the results. The created models were used to compare the impacts of several temperature ranges (ambient, 160°C, and 200°C) for a more thorough analysis.

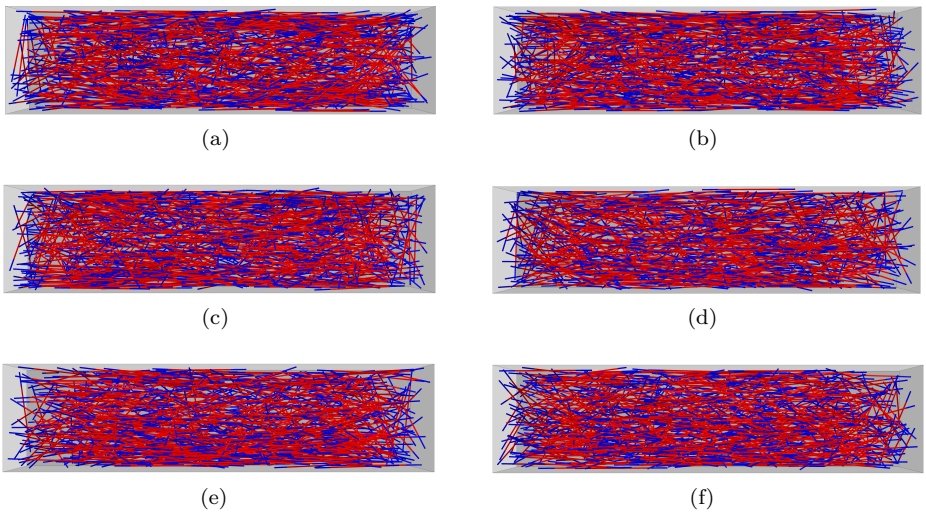

Figure 12: Generated models for subsequent numerical analysis (blue sections represent the end-hooked parts, while red sections denote the straight middle parts of the fibers): (a)–(c) without fiber settlement and (d)–(f) with approximately 5% fiber settlement.

4.2. Constitutive models of materials

For the simulations conducted in ABAQUS CAE, two material components were defined: the concrete matrix and Fe-SMA. This section provides a detailed overview of the fundamental properties and mathematical formulations of these materials. To characterize the mechanical behavior

of the concrete, it was assumed to be isotropic and homogeneous. The Concrete Damage Plasticity (CDP) model, developed by Lubliner [60], Lee, and Fenves [61], was utilized to investigate the behavior of semi-brittle materials. The uniaxial stress-strain relationships of concrete under compressive and tensile loads are illustrated in Figure 13.

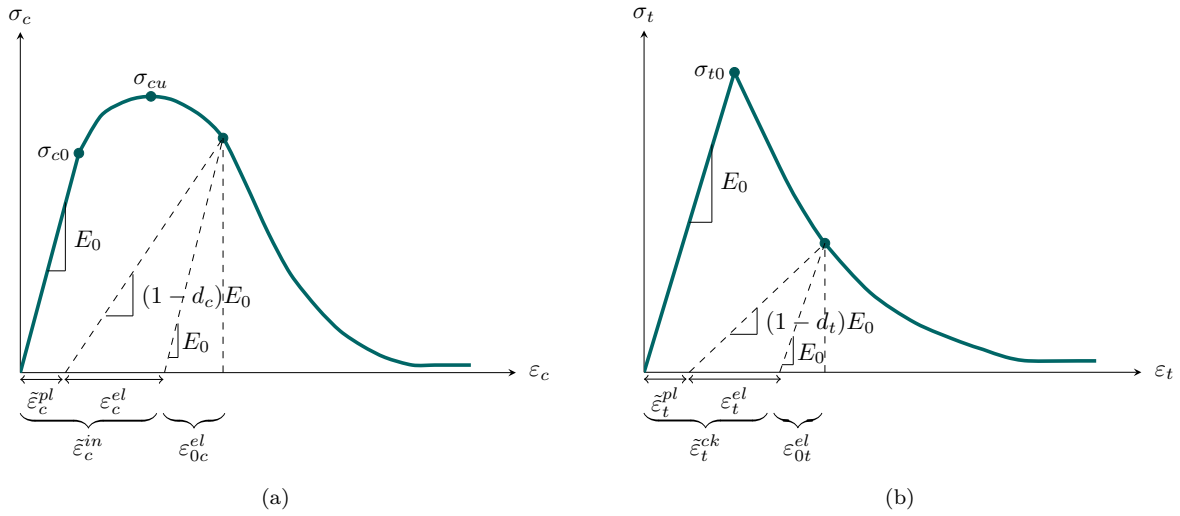

Figure 13: CDP modeling approach depicting the uniaxial stress–strain behavior of semi-brittle materials: (a) compression and (b) tension.

The CDP model's uniaxial tensile and compressive responses are described by the stress-strain relationships given below.

$$\sigma_t = (1-d_t)\,E_0\left(\varepsilon_t - \tilde{\varepsilon}_t^{pl}\right) \tag{1}$$

$$\sigma_c = (1-d_c)\,E_0\left(\varepsilon_c - \tilde{\varepsilon}_c^{pl}\right) \tag{2}$$

The compressive and tensile plastic strains are represented by $\tilde{\varepsilon}_c^{pl}$ and $\tilde{\varepsilon}_t^{pl}$, respectively. The compressive plastic strain, $\tilde{\varepsilon}_c^{pl}$, is defined as the total compressive strain ε_c minus the elastic strain of the undamaged material $\varepsilon_{0c}^{el} = \frac{\sigma_c}{E_0}$, and further reduced by the product of the compressive stress σ_c and a factor dependent on the compressive softening coefficient d_c and the initial elastic modulus E_0. Similarly, the tensile plastic strain, $\tilde{\varepsilon}_t^{pl}$, is calculated by subtracting the elastic strain of the undamaged material $\varepsilon_{0t}^{el} = \frac{\sigma_t}{E_0}$ from the total tensile strain ε_t, and then subtracting the product of the tensile stress σ_t and a term that depends on the tensile softening coefficient d_t and the initial elastic modulus E_0. The scalar softening coefficients for compression and tension, d_c and d_t, respectively, range between $0 \le d_c \le 1$ and $0 \le d_t \le 1$. They are defined as $d_c = 1 - \frac{\sigma_c}{\sigma_{cu}}$ and $d_t = 1 - \frac{\sigma_t}{\sigma_{t0}}$ for stress-strain states on the softening branch.

Experimental tests revealed that thermal heating significantly affects the properties of concrete. Consequently, three distinct concrete models were developed for this study: HPC-A, HPC-160, and HPC-200 for ambient temperature and two ranges of temperature, 160°C and 200°C, respectively. Using the stress-strain curves obtained from the compressive and flexural behavior of the concrete,

the material inputs for the CDP model were defined to simulate the behavior of the concrete matrix in this study. After establishing the initial data inputs for all concrete models in ABAQUS CAE using the CDP model, cubic and prism specimens were modeled to replicate the experimental setups. The concrete models were then assigned to these specimens to calibrate and validate the inputs for the CDP model. Figure 14a shows the cubic specimen under compressive forces, and Figure 14b depicts a prism model subjected to a three-point bending flexural test. Since no direct tensile tests were conducted on the specimens, the axial tensile strength values for each concrete model were calibrated by minimizing the error between the experimental results and numerical analysis for the prism specimens after validating the compressive strength based on the cubic models. Once both the compressive and tensile strength inputs for each concrete model were validated using the CDP model, these values were utilized for further analysis. Figure 14c and 14d present a comparison between the experimental and numerical results from the investigations. The concrete model demonstrates accurate definition and calibration, closely simulating the experimental tests with negligible differences.

For all concrete models, the modulus of elasticity (E_c) was assumed to be approximately 47.5 GPa. The compressive strengths (f_c) were set at 98 MPa, 71 MPa, and 95 MPa for HPC-A, HPC-160, and HPC-200, respectively. The tensile strengths of concrete (f_t) were assumed to be 8 MPa, 6.5 MPa, and 7.8 MPa for HPC-A, HPC-160, and HPC-200, respectively. A Poisson's ratio of 0.2 was applied to all concrete models. Additionally, the geometric parameters defining the plasticity surface for the concrete matrix were assumed as follows: eccentricity (ε) = 0.1; dilation angle (ψ) = 40°; $\sigma_{b0}/\sigma_{c0} = 1.16$; $K_c = 0.667$; and a viscosity parameter of 1×10^{-10}.

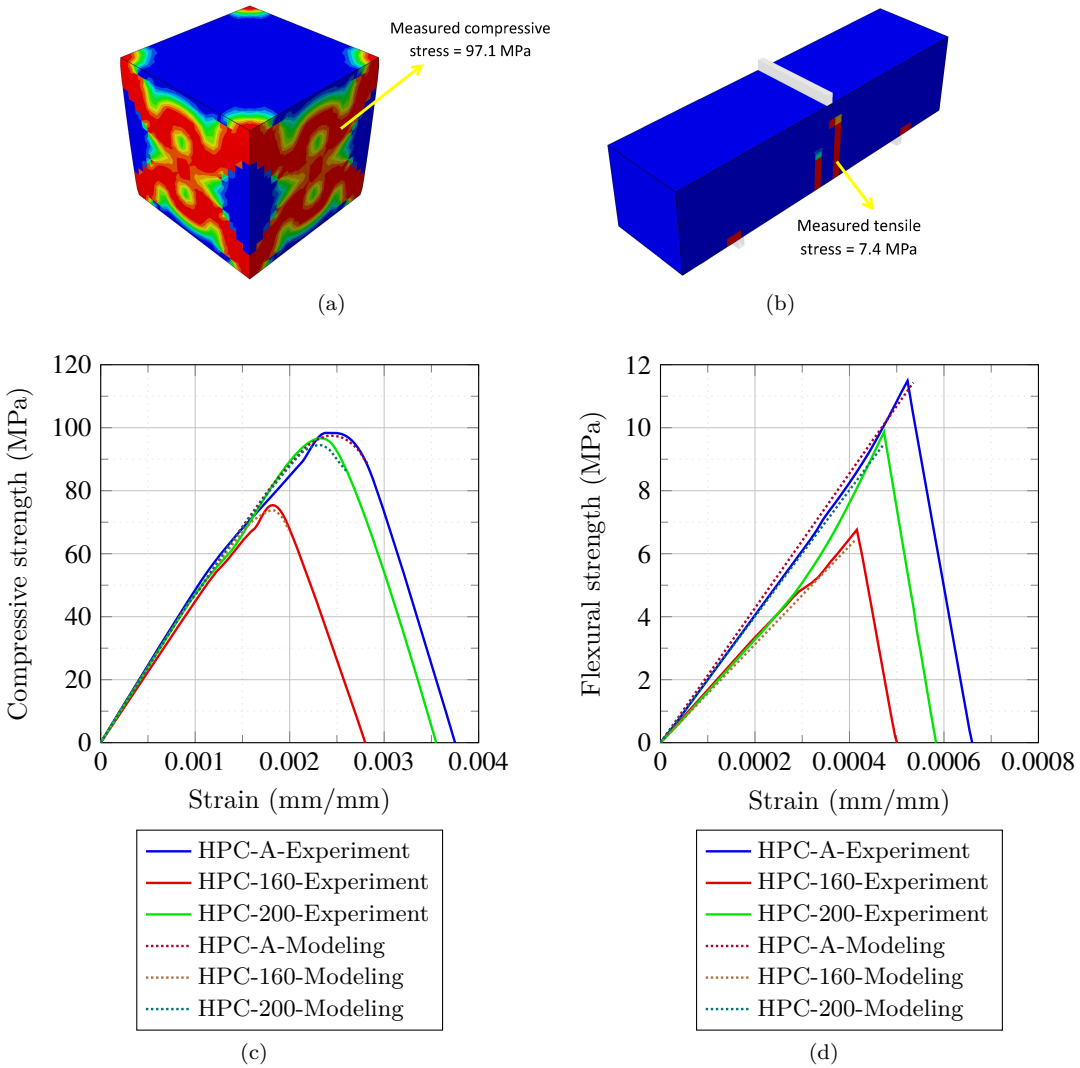

Figure 14: Modeled cubic and prism specimens used to calibrate and validate the CDP inputs for the concrete model: (a) compressive damage and (b) tensile damage (results for the concrete model HPC-A).

To accurately represent the SME property of Fe-SMA in ABAQUS simulations, one of three approaches can be used: using a user material subroutine (UMAT) derived from a robust constitutive model that captures the material's behavior; directly specifying the prestressing stresses; or modeling the temperature effects on the Fe-SMA material as a form of thermal shrinkage. To the authors' knowledge, no current UMATs effectively characterize the complex behavior of Fe-SMA materials.

Previous research by Abouali et al. [62] and Dolatabadi et al. [63] has shown that temperature-dependent models can accurately capture the characteristics of Fe-SMA. Heating Fe-SMA fibers to

160°C results in roughly 360 MPa of recovery force, whereas heating to 200°C results in around 385 MPa of recovery stress. To attain these results, a negative thermal expansion coefficient was established, which allows the material to shrink when heated to the aimed temperature. This thermal shrinkage effectively replicates the recovery stresses generated by the material's phase transformation. Furthermore, the Fe-SMA strips are expected to display isotropic hardening plasticity in their material behavior. According to the literature [64] and empirical studies, the modulus of elasticity of Fe-SMA after activation is around 85 GPa, which is utilized to describe material behavior post-activation. Before activation, the modulus of elasticity is assumed to be 160 GPa. The Poisson's ratio and yield stress are defined at 0.275 and 500 MPa, respectively. The ultimate stress and strain are specified as 1,125 MPa and 22.5%, respectively.

After establishing all input parameters, two Fe-SMA fibers were modeled under configurations identical to the experimental setup, such as boundary conditions, loading rate, and other key variables. Figure 15a shows how the Fe-SMA fiber models respond to thermal heating at 160°C and 200°C. The model accurately predicts recovery stresses at these temperatures. Figure 15b depicts the mechanical properties of the activated Fe-SMA fiber model. Figures 15c and 15d show the stress distribution in the Fe-SMA fiber model after 160°C and 200°C exposures.

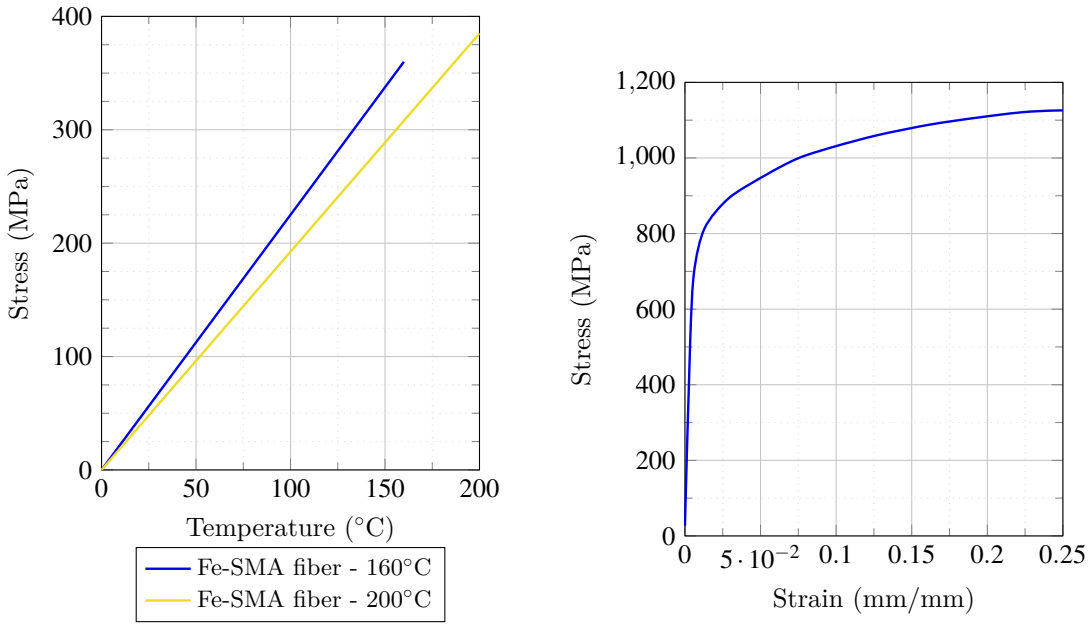

(a) (b)

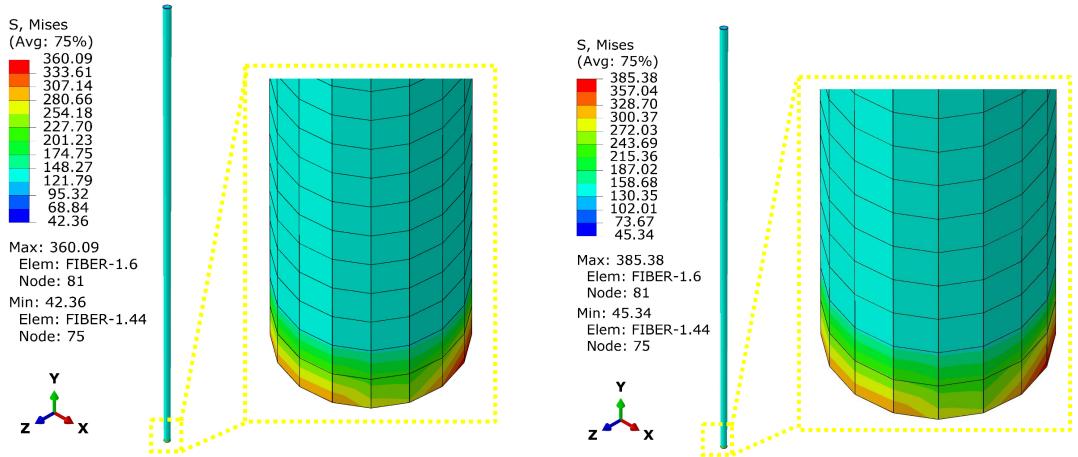

(c) Temperature of 160°C (d) Temperature of 200°C

Figure 15: (a) Thermal behavior under heat exposure, (b) mechanical behavior post-heating as defined for the modeling of Fe-SMA fibers, (c) and (d) the simulation of the Fe-SMA fiber exposed to 160°C and 200°C thermal heating, respectively (units are in MPa).

4.3. Contact properties and interactions

Accurate modeling of the pull-out behavior of Fe-SMA fibers embedded in concrete is required to simulate the mechanical performance of FRC composites. This section describes the procedure used to translate empirical data to numerical input for the simulation, including the constitutive relationships and input data to define the contact properties between Fe-SMA fibers and concrete

matrix. The fibers are represented as straight components in the simulation, with a total length of 35 mm, consisting of a 23 mm central section and two 6 mm end regions (see Figure 16). The end regions represent the mechanical anchoring effect of the actual end-hooked fibers. The end regions and the center area have different contact properties to represent the different interactions with the concrete matrix. The contact properties attributed to the end regions represent the enhanced bonding caused by the end hooks. The middle section's contact properties correspond to straight fibers.

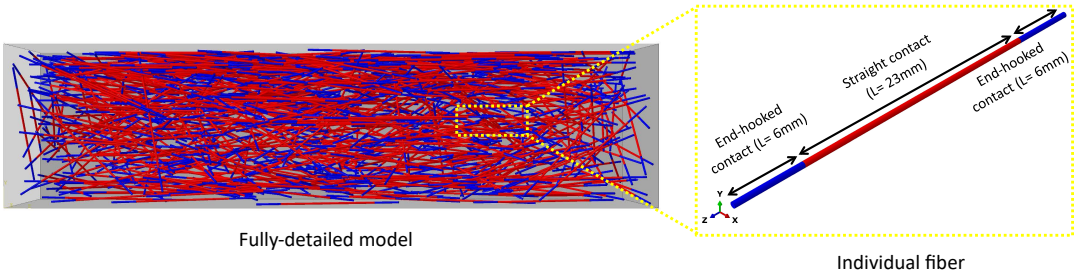

Figure 16: Partitioned straight fiber with distinct contact properties assigned to each segment: end sections (6 mm) resembling end-hooked properties and the central section (23 mm) exhibiting straight fiber contact properties.

Tangential behavior determines frictional resistance at the fiber-concrete interface. The equation is $\tau = \mu p$, where τ is the shear stress, μ is the friction coefficient, and p is the contact pressure (normal stress). In this investigation, a nominal friction coefficient of μ =0.1 is employed. The cohesive behavior specified the bonding and debonding process at the interface using a traction-separation law. The correlation between traction stresses and separations in both normal and shear directions is defined as:

$$\begin{bmatrix} t_n \\ t_s \\ t_t \end{bmatrix} = \begin{bmatrix} K_{nn} & 0 & 0 \\ 0 & K_{ss} & 0 \\ 0 & 0 & K_{tt} \end{bmatrix} \begin{bmatrix} \delta_n \\ \delta s \\ \delta_t \end{bmatrix} \tag{3}$$

where t_n, t_s, t_t are the traction stresses in the normal and two shear directions, δ_n, δ_s, δ_t are the separations in the normal and two shear directions, and K_{nn}, K_{ss}, K_{tt} are the stiffness coefficients in the normal and shear directions. The stiffness matrix is uncoupled, which means there is no interaction between normal and shear behaviors. Due to a lack of particular shear data, shear stiffnesses are assumed to be proportional to normal stiffness: $K_{ss} = K_{tt} = \beta_s K_{nn}$, with β_s=0.8. Damage initiation is determined by the maximum nominal stress threshold. Damage is expected to initiate when the maximum nominal stress ratio reaches unity:

$$\max\left(\frac{\langle t_n \rangle}{\sigma_{\max}}, \frac{t_s}{\tau_{\max}}, \frac{t_t}{\tau_{\max}}\right) = 1 \tag{4}$$

where $\langle t_n \rangle$ is the Macaulay bracket indicating that only tensile normal stresses contribute to damage initiation, $\sigma_{\max}$ and $\tau_{\max}$ are the maximum allowable normal and shear stresses, respectively. Because the fibers are exposed to tensile pull-out without considerable shear, we concentrate on the normal stress component, and shear components are neglected or assumed to be equivalent to the normal component as necessary. The progression of damage after initiation is approximated using

an exponential softening regulation dependent on the displacement (separation):

$$t = t_0 \exp\left(-\beta \frac{\delta - \delta_0}{\delta_f - \delta_0}\right) \tag{5}$$

where t is the current traction stress, t_0 is the traction stress at damage initiation, δ is the current separation, δ_0 is the separation at damage initiation, δ_f is the separation at complete failure, and β is the exponential softening parameter (assumed as 1.0). Friction coefficient for all models was assumed as 0.1.

The parameters required for establishing the contact properties were calculated using empirical force-displacement data provided by Tabrizikahou et al. [42]. Table 3 shows the contact properties between fibers and concrete matrix, based on empirical data applied to the aforementioned formulations and relationships.

Table 3: Input values used to define the contact properties for modeling.

	End regions			Middle Part		
Parameter	Ambient	160°C	200°C	Ambient	160°C	200°C
Friction Coefficient μ				0.1		
Normal Stiffness K_{nn} (N/mm^3)	308.6	154.6	86.3	28.16	17.49	4.98
Shear Stiffness K_{ss}, K_{tt} (N/mm^3)	246.88	123.68	69.04	22.528	13.992	3.984
Maximum Normal Stress $\sigma_{\max}$ (N/mm^2)	33.33	23.36	14.65	4.96	3.15	3.52
Displacement at Failure δ_f (mm)	14.8	14.2	13.4	4.73	4.79	4.49
Exponential Parameter β				1		
Viscosity Coefficient				0.0001		

To validate and verify the procedures and inputs used to define the contact properties, computational modeling was conducted to simulate the fiber pull-out tests. Therefore, a model with identical concrete and Fe-SMA material properties was defined, with a straight fiber embedded within the concrete matrix. Considering the test's symmetrical nature, the model was developed with symmetry boundary conditions to reduce computational time by minimizing the number of elements. Figure 17a shows the meshed model used to numerically analyze the Fe-SMA fiber pull-out. It can be seen that after the fiber is pulled out, stress concentrations in the concrete mainly occur in regions with stronger contact properties, representing the end-hooked geometry. In contrast, the concrete matrix surrounding the straight part of the fiber exhibits lower stress values. Additionally, the plastic strain distribution in the concrete indicates residual strains in the areas corresponding to the end-hooked geometry after fiber pull-out. Figure 17b compares the numerical simulation results with the experimental data. The comparison demonstrates that the model accurately predicts the maximum fiber pull-out resistance. The results show the reliability of the procedures and contact property definitions used for modeling the interaction between Fe-SMA fibers and the concrete matrix.

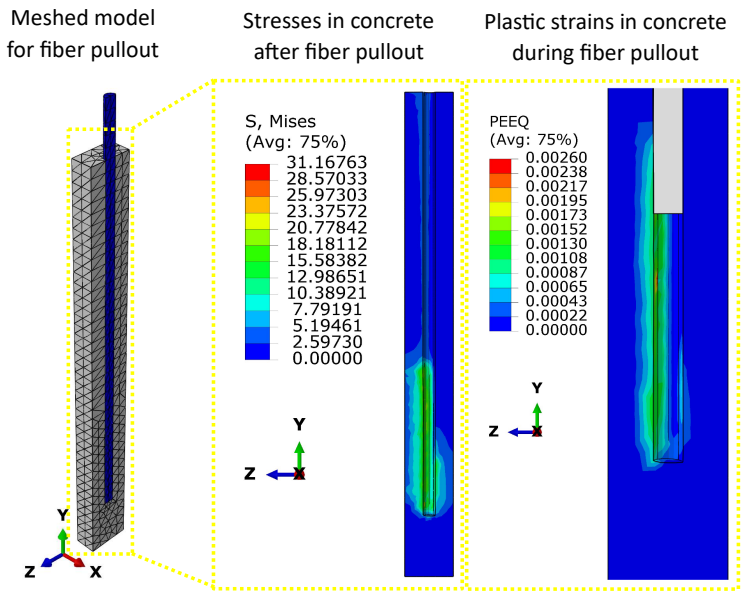

(a)

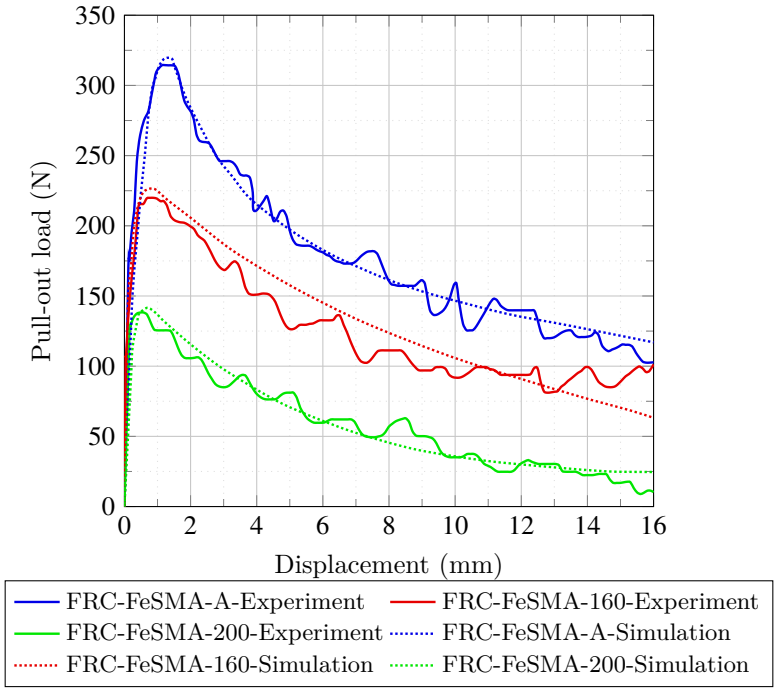

(b)

Figure 17: (a) Simulation of straight Fe-SMA fiber pull-out with different contact properties: 6 mm at the ends to represent end-hooked geometry and 23 mm for the straight part of the fiber, (b) comparison of Fe-SMA fiber pull-out results between experiments [42] and the simulations.

4.4. Validation and mesh sensitivity analysis

After defining, calibrating, and validating all required input data for the computational modeling of concrete prisms reinforced with short Fe-SMA fibers, a mesh sensitivity analysis was conducted to evaluate the model's mesh dependency and determine the optimal mesh size that yields reliable results compared to experimental data. Four different mesh sizes for both the fiber and prism were considered for this analysis. The mesh sizes for the prism elements ranged from a coarse mesh of 10 mm to a fine mesh size of 1.25 mm, while for the fibers, mesh sizes ranged from 2 mm to 0.25 mm. For both the fiber and prism elements, the C3D8R element type (8-node linear brick, reduced integration) was utilized. Table 4 describes the four distinct groups of mesh sizes used for the prism and fibers and Figure 18 illustrates the mesh sizes used in this analysis. The computational modeling was performed on a computer system equipped with an AMD® Ryzen™ 7-4800 CPU 2.90 GHz and 64 GB RAM. For models subjected to ambient temperature (without thermal heating), the calculation times were 11 hours, 29 hours, 51 hours, and 127 hours for Case-1, Case-2, Case-3, and Case-4, respectively. For models with applied heat (160°C and 200°C), the mean analysis times were approximately 15 hours, 38 hours, 92 hours, and 201 hours for Cases 1 through 4, respectively.

Table 4: Mesh sizes and element numbers for prism and fiber models used in mesh sensitivity analysis and model validation.

	Beam		Fiber		
Case	Mesh size (mm)	Elements	Mesh size (mm)	Elements	Total elements
1	10	352	2	53,640	53,992
2	5	2432	1	104,300	106,732
3	2.5	17,408	0.5	208,600	226,008
4	1.25	131,072	0.25	417,200	548,272

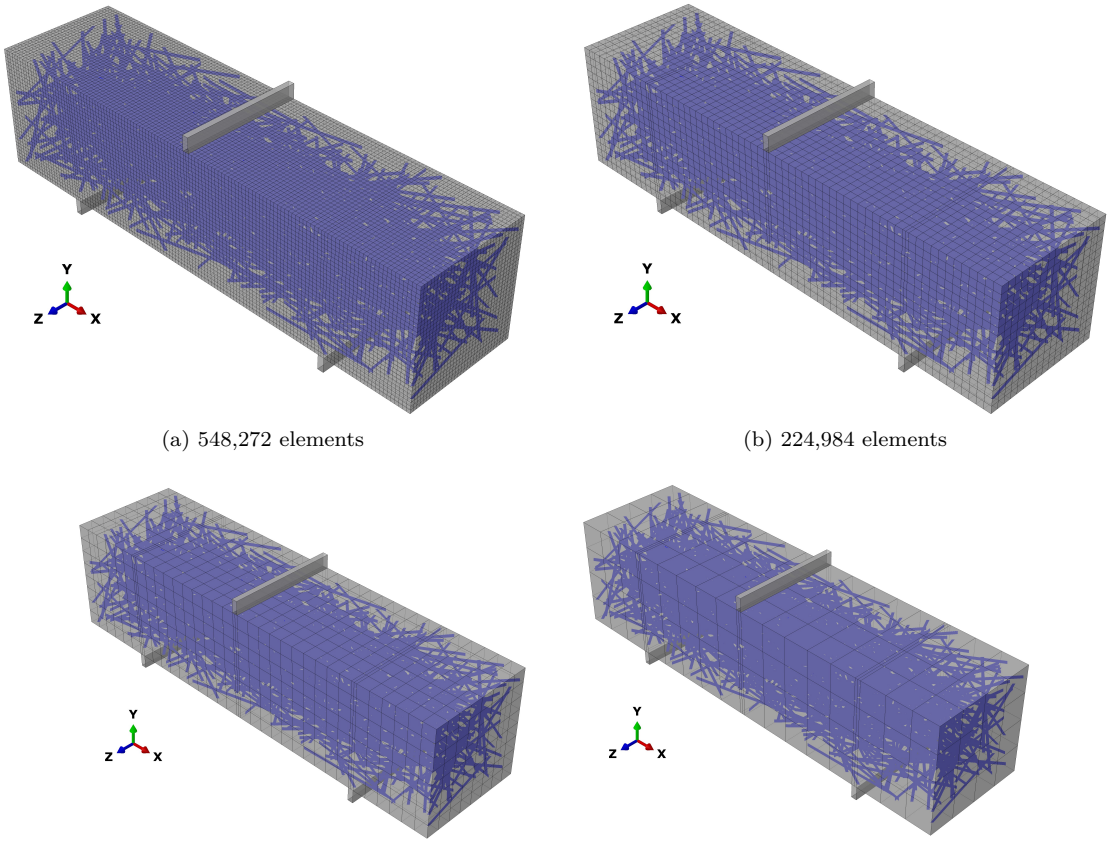

(a) 548,272 elements (b) 224,984 elements

(c) 106,348 elements (d) 53,896 elements

Figure 18: Models with different mesh sizes used for mesh sensitivity analysis: (a) Case-1, (b) Case-2, (c) Case-3, and (d) Case-4.

Figure 19 compares the experimental results with the numerical analysis results obtained using the different mesh sizes. Figure 19a related to specimens without thermal heating (ambient temperature). It can be seen that mesh sizes of 5 mm and 10 mm yield unreliable results, whereas finer mesh sizes of 1.25 mm and 2.5 mm produce more accurate outcomes. Considering the 76-hour difference in computation time and the identical agreement of results within acceptable ranges, a mesh size of 2.5 mm is recommended as it provides accurate results within a reasonable time frame. In Figure 19b and 19c, it is also observed that mesh sizes of 5 mm and 10 mm provide unreliable results, particularly for models subjected to 200°C thermal heating, which show considerable discrepancies compared to experimental data. For finer mesh sizes, the results are reasonable, with only slight differences in predicting the maximum flexural strength of the specimens.

Overall, mesh sizes used in Case-3 (2.5 mm for the prism and 0.5 mm for the fiber) are considered optimal for this analysis, as they yield reliable results comparable to the finer mesh sizes used in Case-4 (1.25 mm for the prism and 0.25 mm for the fiber) while reducing computation time by more than half. It is also important to note, as mentioned previously in Section 4.1, that two groups

of models were analyzed in the numerical analysis: one without fiber settlement and one with 5% fiber settlement. The results presented in Figure 19 pertain to the 5% fiber settlement models. Generally, models without fiber settlement exhibited approximately 12-15% lower flexural strength compared to models with fiber settlement. This outcome was expected, as experiments indicated that the bottom part of the prism contains more fibers, placing more fibers in regions subjected to higher tensile stresses, thereby enhancing resistance to these tensile forces. In contrast, models with homogenized distribution had fewer fibers in the tensile zones, resulting in weaker performance compared to models with a slightly higher concentration of fibers settled at the bottom of the prism.

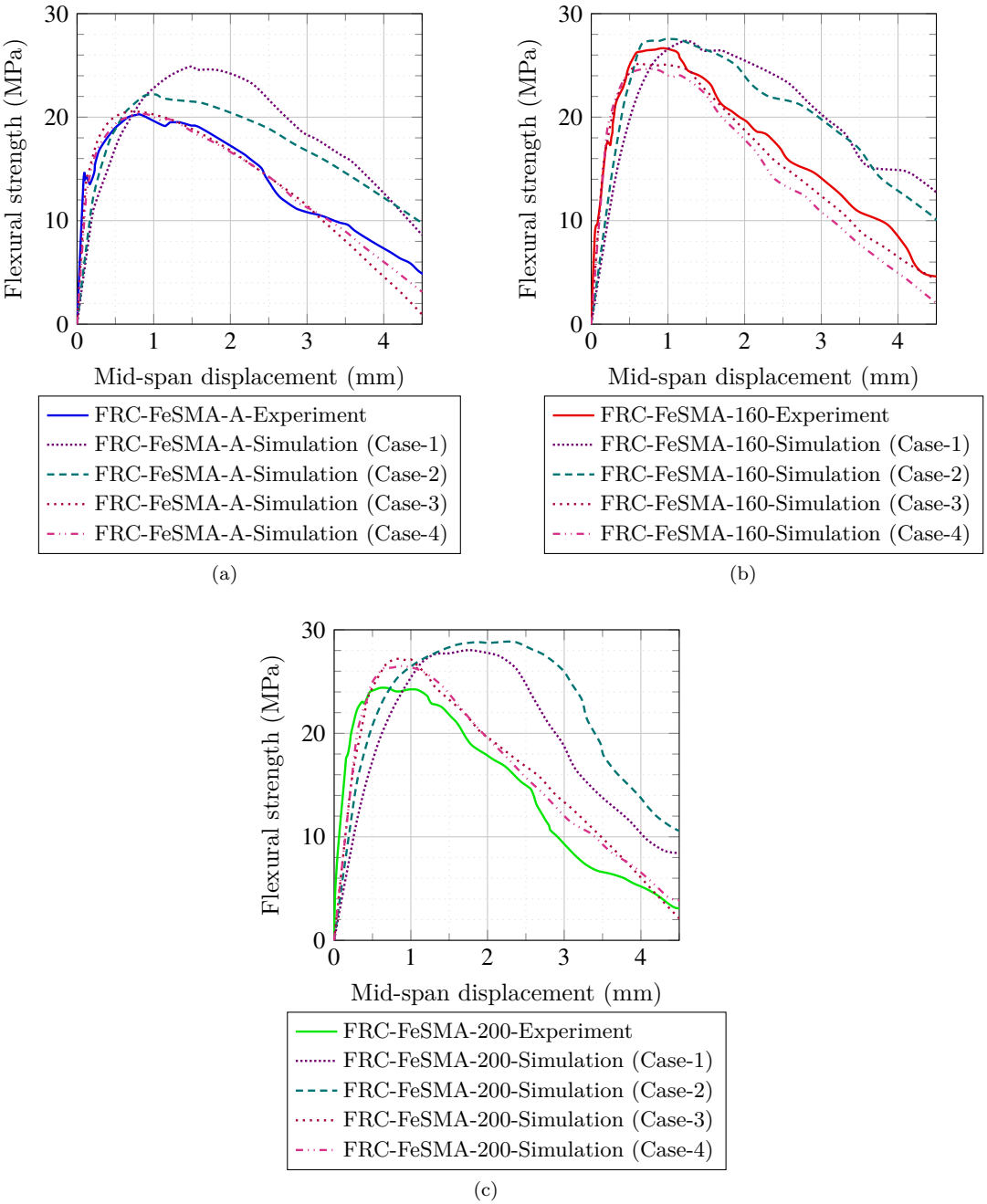

Figure 19: Comparison of experimental and numerical flexural responses of concrete prisms reinforced with Fe-SMA fibers under three-point bending tests, utilizing different mesh sizes (as detailed in Table 4 and Figure 18), for specimens subjected to (a) ambient temperature (reference), (b) 160°C, and (c) 200°C thermal heating.

Figure 20a and 20b illustrate the compressive stress distribution within the concrete matrix of the prism specimens reinforced with embedded short Fe-SMA fibers after thermal heating to 160°C and 200°C, respectively. Laboratory tests (Section 3) revealed that heating Fe-SMA fibers to 200°C in air resulted in approximately 25 MPa greater recovery stress than those heated to 160°C. To define the thermal behavior of the Fe-SMA material for the modeling phase, identical conditions were used for reproducing the experimental results. Concrete specimens with Fe-SMA fibers activated at 200°C showed about 1.2 MPa greater prestressing stresses than those heated at 160°C. However, it was previously discovered that after heating and undergoing three-point bending tests, these specimens exhibited lower flexural strength. This reduction in flexural strength may be related to significantly lower pull-out resistance and weaker adhesion between the concrete matrix and Fe-SMA fibers in specimens exposed to 200°C compared to those exposed to 160°C.

Figure 21a depicts the stress distribution within the Fe-SMA fibers. It is visible that the maximum stress values in the fibers, located at the mid-span, remain well below their plasticity limits. Figure 21b shows the tensile damage distribution in the concrete matrix following a three-point bending test. The crack patterns are similar to those seen in experimental tests (such as in Figure 9), exhibiting asymmetry due to the random distribution of fibers and the initiation of cracks at weaker points within the matrix. Additionally, slight damage occurred near the supports, based on compressive forces, mirroring observations from the experimental tests.

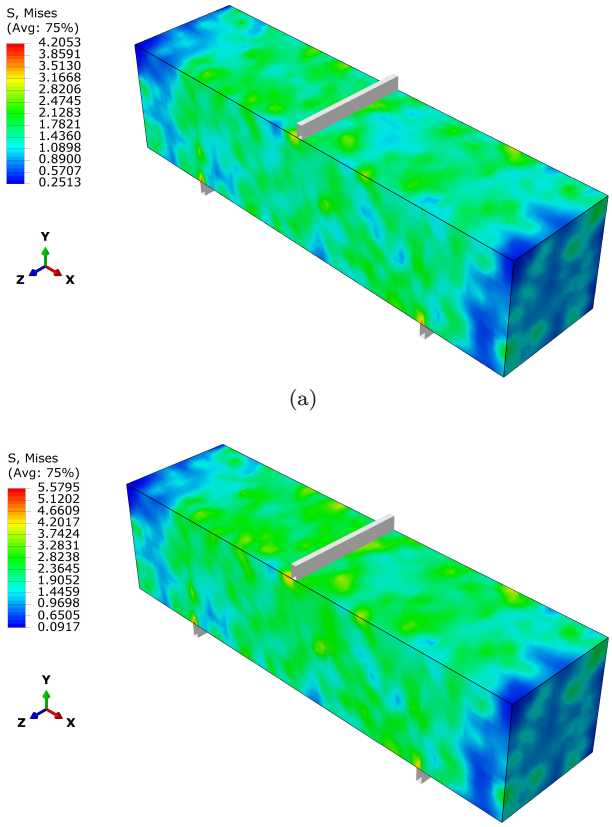

Figure 20: Compressive stress distribution in the concrete matrix generated based on the recovery stresses by Fe-SMA fibers exposed to thermal heating of (a) 160°C, and (b) 200°C.

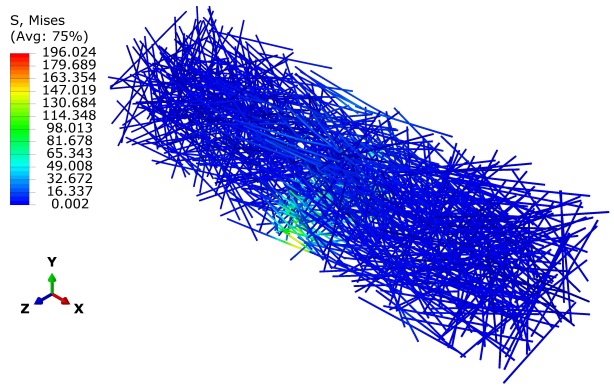

(a)

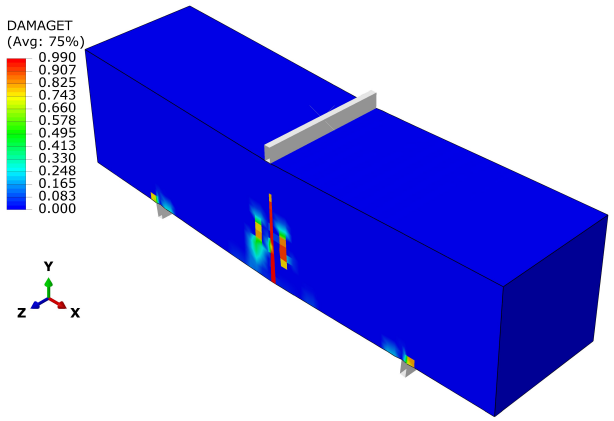

(b)

Figure 21: (a) Stress distribution in Fe-SMA fibers embedded in the concrete prism under three-point bending (b) tensile damage concentration in the concrete matrix with Fe-SMA fibers under three-point bending.

5. Conclusions and final remarks

This study conducted an experimental and numerical analysis to investigate the efficiency of prestressing concrete using short Fe-SMA fibers. Three types of concrete specimens were compared: those reinforced with Fe-SMA fibers, those reinforced with steel fibers, and unreinforced plain concrete. Three-point bending tests were conducted on each group of specimens following exposure to three temperature conditions: ambient (without thermal heating), 160°C, and 200°C. All fiber-reinforced prisms were designed to have a targeted fiber volume fraction of 2%, using fibers with end-hooked geometry to improve pull-out resistance. Based on the obtained results, the following conclusions and remarks can be made:

- Unreinforced plain concrete specimens exposed to heating at 160°C exhibited lower compressive and flexural strengths, measuring 71.7 MPa (a decrease of about 27.1%) and 6.82 MPa (a decrease of about 40.7%), respectively, when compared to those maintained at ambient temperatures, which had compressive and flexural strengths of 98.35 MPa and 11.5 MPa.

However, increasing the temperature from 160°C to 200°C resulted in a minimal reduction in compressive and flexural strengths, reducing them to 95.39 MPa (a decrease of about 3.0%) and 9.88 MPa (a decrease of about 14.1%), respectively. This observation highlights the need for further research to fully understand the underlying mechanisms that drive these changes.

- In three-point bending tests, unheated concrete specimens reinforced with Fe-SMA fibers exhibited a decrease in flexural strength of approximately 2.75 MPa (about 12.0%) compared to those reinforced with steel fibers. However, the thermally activated Fe-SMA-reinforced specimens demonstrated greater flexural strength than the steel fiber-reinforced specimens, as the flexural strength of the latter decreased with increasing temperature. Thermal activation at temperatures ranging from 160°C to 200°C is expected to increase the recovery stress of Fe-SMA fibers by about 25 MPa (about 6.5%) when activated in air. Nevertheless, this increase was not observed when the fibers were used in concrete; instead, a slight reduction of 2.26 MPa (about 4.8%) was measured. Notably, Fe-SMA-reinforced specimens heated to 160°C showed higher flexural strength with 26.65 MPa than those heated to 200°C with 24.39 MPa. This discrepancy may be attributed to a reduction in pull-out resistance and the negative impacts of thermal heating on fiber-matrix interactions as well as concrete material characteristics. Therefore, an optimal activation temperature of 160°C is recommended to provide adequate prestressing stresses while minimizing adverse effects.

- The reduction in flexural strength at higher activation temperatures (specifically, 160°C and 200°C in this study) is likely due to the negative effects of thermal heating on the pull-out resistance between the Fe-SMA fibers and the concrete matrix. Enhancing the pull-out resistance between Fe-SMA fibers and the concrete matrix remains an important goal. To achieve this, future efforts could focus on optimizing the alloy composition or processing conditions of Fe-SMA fibers to lower their required activation temperature, thereby reducing thermal degradation effects. Additionally, fine-tuning the concrete mix design or employing short-duration, localized heating methods may help maintain better fiber–concrete bonding during activation, ultimately improving the overall performance of Fe-SMA-reinforced systems. Future research should focus on investigating alternative fiber end geometries that improve pull-out resistance, and consider other viable solutions to address this issue.

- An algorithm was developed to randomly distribute Fe-SMA fibers within concrete while preventing their intersections and placement at specimen boundaries. Empirical data defined the contact properties of fiber-concrete interactions. To simplify the end-hooked geometry, fibers were modeled as straight elements with modified end-contact characteristics, effectively reproducing pull-out behavior. Concrete was defined using the CDP model, and a negative thermal expansion coefficient captured the Fe-SMA phase transformation and associated recovery stresses. Although this approach worked well, a more advanced constitutive model is required to fully understand complex behaviors like early thermal expansion and potential microcracking. Moreover, the required finite element models are computationally expensive: small specimens with 750 fibers take days to simulate, making direct modeling of millions of fibers impractical. Future research should consider homogenization techniques, analytical formulations, and multiscale/multiphysics methods for improved efficiency [65].

- While heating weakened plain concrete, thermally activated Fe-SMA-reinforced specimens showed improved flexural strength due to the fibers' shape recovery. Adjusting the concrete mix design could further enhance these gains. However, fully heating large elements like bridge

columns may be impractical. Future research should explore selective activation methods or optimize alloy compositions to lower activation temperatures. Such strategies could maintain concrete integrity and offer cost- and time-effective solutions for larger, more complex structures.

- This study shows that short Fe-SMA fibers can effectively prestress concrete, increasing flexural strength by about 24.2% at 160°C and 17.2% at 200°C for a 2.0% fiber volume fraction, comparing to reference specimens (without heating). Future work could explore using these fibers to enable fracture closure and self-healing. While NiTi-based systems offer similar benefits, Fe-SMA fibers are more cost-effective and scalable. By activating the fibers after cracking, the induced prestress can bring cracked surfaces together, reducing crack widths and potentially improving durability in large-scale infrastructure applications.

Author contributions

Alireza Tabrizikahou – Conceptualization, Formal analysis, Investigation, Methodology, Project administration, Validation, Visualization, Writing – original draft. Mieczysław Kuczma – Resources, Supervision, Writing – review and editing. Zafiris Triantafyllidis – Formal analysis, Investigation, Writing – review and editing. Moslem Shahverdi – Resources, Supervision, Writing – review and editing

Declaration of competing interest

The authors declare that they have no known competing financial interests or personal relationships that could have appeared to influence the work reported in this paper.

Data availability

Data will be made available on request.

Acknowledgements

This research was partially funded by the National Science Centre of Poland (Grant No. 2023/49/N/ST8/03063). The authors are also grateful to the Ernst Göhner Foundation in Switzerland, re-fer AG (with particular thanks to Dr. Julien Michels), the Structural Engineering Research Laboratory of Empa, and Dr. Mateusz Wyrzykowski from the Concrete and Asphalt Laboratory of Empa, for providing financial, scientific and technical support for this research study.

Declaration of generative AI and AI-assisted technologies in the writing process

During the preparation of this work, the authors used Generative Pre-trained Transformer 4 (GPT-4) to improve language and readability. After using this tool, the authors reviewed and edited the content as needed and took full responsibility for the content of the publication.

References

[1] Y. Huang, S. Grünewald, E. Schlangen, M. Luković, Strengthening of concrete structures with ultra high performance fiber reinforced concrete (UHPFRC): A critical review, Construction and Building Materials 336 (2022) 127398. doi:10.1016/j.conbuildmat.2022.127398.

[2] H. Khalel, M. Khan, A. Starr, K. A. Khan, A. Muhammad, Performance of engineered fibre reinforced concrete (EFRC) under different load regimes: A review, Construction and Building Materials 306 (2021) 124692. doi:10.1016/j.conbuildmat.2021.124692.

[3] M. Al-Zu'bi, M. Fan, L. Anguilano, Advances in bonding agents for retrofitting concrete structures with fibre reinforced polymer materials: A review, Construction and Building Materials 330 (2022) 127115. doi:10.1016/j.conbuildmat.2022.127115.

[4] Y. Zheng, Y. Zhang, J. Zhuo, Y. Zhang, C. Wan, A review of the mechanical properties and durability of basalt fiber-reinforced concrete, Construction and Building Materials 359 (2022) 129360. doi:10.1016/j.conbuildmat.2022.129360.

[5] A. A. El-Abbasy, Tensile, flexural, impact strength, and fracture properties of ultra-high-performance fiber-reinforced concrete – A comprehensive review, Construction and Building Materials 408 (2023) 133621. doi:10.1016/j.conbuildmat.2023.133621.

[6] H. Wu, A. Shen, G. Ren, Q. Ma, Z. Wang, Q. Cheng, Y. Li, Dynamic mechanical properties of fiber-reinforced concrete: A review, Construction and Building Materials 366 (2023) 130145. doi:10.1016/j.conbuildmat.2022.130145.

[7] D.-Y. Yoo, Y.-S. Yoon, A Review on Structural Behavior, Design, and Application of Ultra-High-Performance Fiber-Reinforced Concrete, International Journal of Concrete Structures and Materials 10 (2) (2016) 125–142. doi:10.1007/s40069-016-0143-x.

[8] J. Gong, Y. Ma, J. Fu, J. Hu, X. Ouyang, Z. Zhang, H. Wang, Utilization of fibers in ultra-high performance concrete: A review, Composites Part B: Engineering 241 (2022) 109995. doi:10.1016/j.compositesb.2022.109995.

[9] V. Afroughsabet, L. Biolzi, T. Ozbakkaloglu, High-performance fiber-reinforced concrete: a review, Journal of Materials Science 51 (14) (2016) 6517–6551. doi:10.1007/s10853-016-9917-4.

[10] P. Rossi, High performance multimodal fiber reinforced cement composites (hpmfrcc): The lcpc experience, Materials Journal 94 (6) (1997) 478–783.

[11] B. A. Graybeal, et al., Material property characterization of ultra-high performance concrete, Tech. rep., United States. Federal Highway Administration. Office of Infrastructure … (2006).

[12] K. Wille, A. E. Naaman, G. J. Parra-Montesinos, Ultra-high performance concrete with compressive strength exceeding 150 mpa (22 ksi): A simpler way., ACI materials journal 108 (1) (2011).

[13] D. C. Lagoudas, J. G. Boyd, Z. Bo, Micromechanics of active composites with SMA fibers, Journal of Engineering Materials and Technology 116 (1994) 337–347. doi:10.1115/1.2904297.

[14] A. Tabrizikahou, M. Kuczma, M. Łasecka-Plura, E. Noroozinejad Farsangi, M. Noori, P. Gardoni, S. Li, Application and modelling of Shape-Memory Alloys for structural vibration control: State-of-the-art review, Construction and Building Materials 342 (2022) 127975. doi:10.1016/j.conbuildmat.2022.127975.

[15] A. Tabrizikahou, M. Kuczma, C. Czaderski, M. Shahverdi, From experimental testing to computational modeling: A review of shape memory alloy fiber-reinforced concrete composites, Composites Part B: Engineering 281 (2024) 111530. doi:10.1016/j.compositesb.2024.111530.

[16] M. S. Saiidi, H. Wang, Exploratory study of seismic response of concrete columns with shape memory alloys reinforcement, ACI Materials Journal 103 (3) (2006) 436.

[17] M. S. Saiidi, M. O'Brien, M. Sadrossadat-Zadeh, Cyclic response of concrete bridge columns using superelastic nitinol and bendable concrete., ACI Structural Journal 106 (1) (2009).

[18] M. S. Saiidi, M. Sadrossadat-Zadeh, C. Ayoub, A. Itani, Pilot study of behavior of concrete beams reinforced with shape memory alloys, Journal of Materials in Civil Engineering 19 (2007) 454–461. doi:10.1061/(ASCE)0899-1561(2007)19:6(454).

[19] O. E. Ozbulut, S. Hurlebaus, A comparative study on the seismic performance of superelastic-friction base isolators against near-field earthquakes, Earthquake Spectra 28 (3) (2012) 1147–1163.

[20] E. Choi, A. Ostadrahimi, W. J. Kim, Enhancement of compressive strength and strain ductility of SMA fiber reinforced concrete considering fiber's aspect ratios, Construction and Building Materials 345 (2022) 128346. doi:10.1016/j.conbuildmat.2022.128346.

[21] A. Dehghani, F. Aslani, Flexural toughness and compressive stress–strain behaviour of pseudoelastic shape memory alloy fibre reinforced concrete, Construction and Building Materials 332 (2022) 127372. doi:10.1016/j.conbuildmat.2022.127372.

[22] A. Dehghani, F. Aslani, Advanced shape memory alloy fibers designed to enhance crack closure and re-centring performance in cement-based composites, Construction and Building Materials 415 (2024) 135095. doi:10.1016/j.conbuildmat.2024.135095.

[23] J.-H. Lee, E. Choi, J.-S. Jeon, Experimental investigation on the performance of flexural displacement recovery using crimped shape memory alloy fibers, Construction and Building Materials 306 (2021) 124908. doi:10.1016/j.conbuildmat.2021.124908.

[24] D. W. Menna, A. S. Genikomsou, M. F. Green, Flexural performance and crack closing capacity of double-hooked-end superelastic shape memory alloy fibre-reinforced concrete beams under cyclic loading using digital image correlation, Construction and Building Materials 409 (2023) 133744. doi:10.1016/j.conbuildmat.2023.133744.

[25] A. Dehghani, F. Aslani, Crack recovery and re-centring performance of cementitious composites with pseudoelastic shape memory alloy fibres, Construction and Building Materials 298 (2021) 123888. doi:10.1016/j.conbuildmat.2021.123888.

[26] L. Janke, C. Czaderski, M. Motavalli, J. Ruth, Applications of shape memory alloys in civil engineering structures—overview, limits and new ideas, Materials and Structures 38 (2005) 578–592. doi:10.1007/BF02479550.

[27] M. Alam, M. Youssef, M. Nehdi, Utilizing shape memory alloys to enhance the performance and safety of civil infrastructure: a review, Canadian Journal of Civil Engineering 34 (9) (2007) 1075–1086.

[28] M. Song, J. Wang, L. Yuan, C. Luan, Z. Zhou, Investigation on crack recovery behavior of engineered cementitious composite (ECC) incorporated memory alloy fiber at low temperature, ES Materials and Manufacturing (2022). doi:10.30919/esmm5f662.

[29] W. Chen, B. Lin, K. Feng, S. Cui, D. Zhang, Effect of shape memory alloy fiber content and preloading level on the self-healing properties of smart cementitious composite (SMA-ECC), Construction and Building Materials 341 (2022) 127797. doi:10.1016/j.conbuildmat.2022.127797.

[30] K.-J. Lee, J.-H. Lee, C.-Y. Jung, E. Choi, Crack-closing performance of niti and nitinb fibers in cement mortar beams using shape memory effects, Composite Structures 202 (2018) 710–718. doi:10.1016/j.compstruct.2018.03.080.

[31] K. Moser, A. Bergamini, R. Christen, C. Czaderski, Feasibility of concrete prestressed by shape memory alloy short fibers, Materials and Structures 38 (5) (2005) 593–600. doi:10.1007/BF02479551.

[32] M. K. Kim, D. J. Kim, Y.-S. Chung, E. Choi, Direct tensile behavior of shape-memory-alloy fiber-reinforced cement composites, Construction and Building Materials 102 (2016) 462–470. doi:10.1016/j.conbuildmat.2015.11.015.

[33] J. Van Humbeeck, Non-medical applications of shape memory alloys, Materials Science and Engineering: A 273 (1999) 134–148. doi:10.1016/S0921-5093(99)00293-2.

[34] G. Song, N. Ma, H.-N. Li, Applications of shape memory alloys in civil structures, Engineering Structures 28 (2006) 1266–1274. doi:10.1016/j.engstruct.2005.12.010.

[35] A. Cladera, B. Weber, C. Leinenbach, C. Czaderski, M. Shahverdi, M. Motavalli, Iron-based shape memory alloys for civil engineering structures: An overview, Construction and building materials 63 (2014) 281–293.

[36] E. Ghafoori, M. Neuenschwander, M. Shahverdi, C. Czaderski, M. Fontana, Elevated temperature behavior of an iron-based shape memory alloy used for prestressed strengthening of civil structures, Construction and Building Materials 211 (2019) 437–452. doi:10.1016/j.conbuildmat.2019.03.098.

[37] C. Czaderski, M. Shahverdi, R. Brönnimann, C. Leinenbach, M. Motavalli, Feasibility of iron-based shape memory alloy strips for prestressed strengthening of concrete structures, Construction and Building Materials 56 (2014) 94–105. doi:10.1016/j.conbuildmat.2014.01.069.

[38] M. Shahverdi, C. Czaderski, M. Motavalli, Iron-based shape memory alloys for prestressed near-surface mounted strengthening of reinforced concrete beams, Construction and Building Materials 112 (2016) 28–38.

[39] M. Shahverdi, J. Michels, C. Czaderski, M. Motavalli, Iron-based shape memory alloy strips for strengthening RC members: Material behavior and characterization, Construction and Building Materials 173 (2018) 586–599. doi:10.1016/j.conbuildmat.2018.04.057.

[40] European Committee for Standardization (CEN), EN 1015–11:2020 Methods of test for mortar for masonry - Part 11: Determination of flexural and compressive strength of hardened mortar (2020).

[41] ASTM International, C192/C192M-19 Standard Practice for Making and Curing Concrete Test Specimens in the Laboratory (2019). doi:10.1520/C0192_C0192M-18.

[42] A. Tabrizikahou, M. Kuczma, M. Shahverdi, Impact of fiber geometry, temperature, loading rate, and concrete mix on the pull-out resistance of iron-based shape memory alloy (Fe-SMA): Experimental investigation, Construction and Building Materials 456 (2024) 139298. doi:10.1016/j.conbuildmat.2024.139298.

[43] Z. Dong, U. E. Klotz, C. Leinenbach, A. Bergamini, C. Czaderski, M. Motavalli, A Novel Fe-Mn-Si Shape Memory Alloy With Improved Shape Recovery Properties by VC Precipitation, Advanced Engineering Materials 11 (1-2) (2009) 40–44. doi:10.1002/adem.200800312.

[44] Z. Triantafyllidis, M. J. Oza, J. Michels, M. Wyrzykowski, M. Shahverdi, Development and characterization of thin iron-based shape memory alloy prestressing wire, Procedia Structural Integrity 64 (2024) 2083–2090. doi:10.1016/j.prostr.2024.09.304.

[45] J. Vůjtěch, P. Ryjáček, J. Campos Matos, E. Ghafoori, Iron-Based shape memory alloy for strengthening of 113-Year bridge, Engineering Structures 248 (2021) 113231. doi:10.1016/j.engstruct.2021.113231.

[46] M. Izadi, E. Ghafoori, M. Shahverdi, M. Motavalli, S. Maalek, Development of an iron-based shape memory alloy (Fe-SMA) strengthening system for steel plates, Engineering Structures 174 (2018) 433–446. doi:10.1016/j.engstruct.2018.07.073.

[47] G. Fawaz, J. Murcia-Delso, Bond behavior of iron-based shape memory alloy reinforcing bars embedded in concrete, Materials and Structures 53 (5) (2020) 114. doi:10.1617/s11527-020-01548-y.

[48] I. Hager, Behaviour of cement concrete at high temperature, Bulletin of the Polish Academy of Sciences: Technical Sciences (1) (2013).

[49] S. Banerji, V. Kodur, Effect of temperature on mechanical properties of ultra-high performance concrete, Fire and Materials 46 (2022) 287–301. doi:10.1002/fam.2979.

[50] I.-H. Yang, J. Park, Mechanical and thermal properties of UHPC exposed to high-temperature thermal cycling, Advances in Materials Science and Engineering 2019 (2019) 1–12. doi:10.1155/2019/9723693.

[51] Y. Zhu, H. Hussein, A. Kumar, G. Chen, A review: Material and structural properties of UHPC at elevated temperatures or fire conditions, Cement and Concrete Composites 123 (2021) 104212. doi:10.1016/j.cemconcomp.2021.104212.

[52] W. Meng, A. Kumar, K. H. Khayat, Effect of silica fume and slump-retaining polycarboxylate-based dispersant on the development of properties of portland cement paste, Cement and Concrete Composites 99 (2019) 181–190. doi:10.1016/j.cemconcomp.2019.03.021.

[53] H. Bahmani, D. Mostofinejad, Microstructure of ultra-high-performance concrete (UHPC) – a review study, Journal of Building Engineering 50 (2022) 104118. doi:10.1016/j.jobe.2022.104118.

[54] G. Ruano, F. Isla, B. Luccioni, R. Zerbino, G. Giaccio, Steel fibers pull-out after exposure to high temperatures and its contribution to the residual mechanical behavior of high strength concrete, Construction and Building Materials 163 (2018) 571–585. doi:10.1016/j.conbuildmat.2017.12.129.

[55] D.-Y. Yoo, S. Kim, J.-J. Kim, B. Chun, An experimental study on pullout and tensile behavior of ultra-high-performance concrete reinforced with various steel fibers, Construction and Building Materials 206 (2019) 46–61. doi:10.1016/j.conbuildmat.2019.02.058.

[56] D. Zhang, J. Jiang, Y. Weng, D. Wang, X. Wu, S. Fan, Pull-out behaviour of steel fibres embedded in ultra-high-performance concrete after exposure to high temperatures, Construction and Building Materials 408 (2023) 133630. doi:10.1016/j.conbuildmat.2023.133630.

[57] W. Huang, B. Huang, A. Pan, Q. Chen, Q. Huang, R. Xu, Y. Yang, F. Xue, Numerical statistics-based research on the spatial distribution of cylindrical fiber in ideal simulated fiber reinforced concrete matrix, Construction and Building Materials 379 (2023) 131209. doi:10.1016/j.conbuildmat.2023.131209.

[58] C. Zhang, P. Liu, K. Li, C. Shi, Generation and property analyses of 3D mesoscale models for plain and fiber reinforced concretes, Cement and Concrete Composites 114 (2020) 103714. doi:10.1016/j.cemconcomp.2020.103714.

[59] H. Mashhadban, S. S. Kutanaei, M. A. Sayarinejad, Prediction and modeling of mechanical properties in fiber reinforced self-compacting concrete using particle swarm optimization algorithm and artificial neural network, Construction and Building Materials 119 (2016) 277–287. doi:10.1016/j.conbuildmat.2016.05.034.

[60] J. Lubliner, J. Oliver, S. Oller, E. Oñate, A plastic-damage model for concrete, International Journal of Solids and Structures 25 (3) (1989) 299–326. doi:10.1016/0020-7683(89)90050-4.

[61] J. Lee, G. L. Fenves, Plastic-Damage Model for Cyclic Loading of Concrete Structures, Journal of Engineering Mechanics 124 (8) (1998) 892–900. doi:10.1061/(ASCE)0733-9399(1998)124:8(892).

[62] S. Abouali, M. Shahverdi, M. Ghassemieh, M. Motavalli, Nonlinear simulation of reinforced concrete beams retrofitted by near-surface mounted iron-based shape memory alloys, Engineering Structures 187 (2019) 133–148. doi:10.1016/j.engstruct.2019.02.060.

[63] N. Dolatabadi, M. Shahverdi, M. Ghassemieh, M. Motavalli, RC Structures Strengthened by an Iron-Based Shape Memory Alloy Embedded in a Shotcrete Layer—Nonlinear Finite Element Modeling, Materials 13 (23) (2020) 5504. doi:10.3390/ma13235504.

[64] N. Khodkari, S. Raza, B. Schranz, Y. E. Harmanci, S. Mohammadi, M. Motavalli, M. Shahverdi, Nonlinear finite element modelling of the bond behavior of near-surface mounted Fe-SMA bars, Structures 66 (2024) 106836. doi:10.1016/j.istruc.2024.106836.

[65] A. Saeedi, A. Tabrizikahou, M. Shahverdi, Study of activation parameters in Fe-SMA reinforced concrete structures using multiphysics modelling, Procedia Structural Integrity 64 (2024) 2044–2050. doi:10.1016/j.prostr.2024.09.294.